Aerodynamic and Aeroacoustic Characteristics of JAXA Real-sized Quiet Rotor Blade

Shigeru Saito, Yasutada Tanabe, Noboru Kobiki
Aviation Program Group, Japan Aerospace Exploration Agency (JAXA)
7-44-1 Jindaiji Higashi-machi, Chofu, Tokyo 182-8522, JAPAN
Tel.(+81) 50-3362-3152, Fax. (+81) 422-40-3235
e-mail: ssaito@chofu.jaxa.jp

Hideaki Sugawara
Engineering Solution Division, Ryoyu Systems Co., LTD.,
6-19 Oe-Machi, Minato-ku, Nagoya, Aichi 455-0024, Japan

Naoto Sasaki, Hajime Fujita
Nihon University,
1-8-14 Kanda Surugadai, Chiyoda-ku, Tokyo, 101-8308, Japan

Abstract

In JAXA, study of the aerodynamic perfomance/dynamics and aeroacoustics for helicopter has been conducted by the two approaches. One is the theoretical approach using the comprehensive code such as Local Momentum Theory/prescribed wake model and numereical simulation approach such as 3D Euler/Navier Stokes code so far. The other is experimental approach using low speed wind tunnel such as JAXA low speed wind tunnel (5.5m width x 6.5m height test section).

In the theoretical approach, the comprehensive code named LMT has applied to investigate several kind of helicopters such as single, tandem and coaxial type helicopters. Also this is used to investigate the dynamic effect of a helicopter by atomoshperic gust and tip vortex generated from a large scale jet airplane. To develop the CFD code, Euler formulation is mainly applied to investigate the flow field around a helicopter rotor, especially to capture the tip vortex generated from blade tip region. In the code, the SLAU scheme was applied to capture the more precise vortex system generated from blade root region, usally the flow speed around a root of a blade is more low compared with the outer region of blade. The effect of elastic deformation of a blade has also been included of this code to obtain the more presice

In the wind tunnel approach, the JAXA multi-purpose rotor test stand (JMRTS) with 2m rotor diameter has been constracted to inestigate the aerodynamic/aeroacoustic performance of a heliccopter. the active device such as an active flap has installed on a rotor blade and tested to evaluate the device performance on trhe areodymaics/aeroacoustics.

Since 2008, the design of a real-isze low noise helicopter rotor blade with the JAXA developed active flap system has started in order to validate the effect of an active flap system. Within the three years, the conceptual design, the engineering study including analytical dynamic evaluation and the bench tests evaluating static, dynamic and endurance performances have been completed.

This paper describes the aerodynamic and aeroacoustic property of JAXA real-size quiet rotor blade (called JLNB) with an active flap at the trailing edge of a blade. The elastic properties, such as natural frrequencies and mode analysis, has been performaed and included in the calculation of aerodynamic/aeroacoustic performance. The adaptive controller has been applied to evaluate the effect of the active flap on the vibration/noise reduction of JLNB.

It is found that the characteristic property of JLNB conducted by the JAXA in-house code named rMode shows the good coincident with that of CAMRAD II. It is also shown that the adaptive controller has good potential to reduce the vibration and noise.

1. Introduction

Helicopters have a great potential to operate in the normal/critical activities such as life-saving, fire-fighting, air rescue, transfortation, police observation, broadcasting from the sky and so on. However due to the noise problem, the operation area or time has been restricted, especially in the urban area (usally more populated area). Therefore the noise reduction problem is most important issue to be solved in the helicopter technology.

The active devices such as higher harmonic control (HHC)[1], individual blade control (IBC)[2, 3], active flap[4-8], active twist[.9, 10], active tab[11-13] etc. are the great means to solve these problem. Recently huge number of research work concerning with these new technologies have been conducted to investigate the effect of these devices on the aerodynamic perfromance, rotor vibratory load reduction and noise such as Blade Vortex Interaction (BVI) noise in the wind tunnel or whirl tower. Boeing has conducted the real-size rotor blade (SMART Rotor) wind tunnel test by NFAC in NASA Ames[14-15]. Eurocopter has developed the real-size low noise rotor blades and conductd the flight test. Two type blades called "blue edge"[16] and "blue pulse"[17-20]. In JAXA, the design of the real-size quiet rotor blade has started since 2009. there has been three stages to conduct this project, one is the conceptual design stage, second step is the engineering study including analytical dynamic evaluation and the third step is the bench tests evaluating static, dynamic and endurance performances. The design features of JAXA quiet rotor blade have been described in ref.[21]. From this conceptual design, the capability of the noise reduction using an active flap has been shown in figure 1. JAXA real-size active flap system can reduce the BVI noise reduction with more than 6 dB.

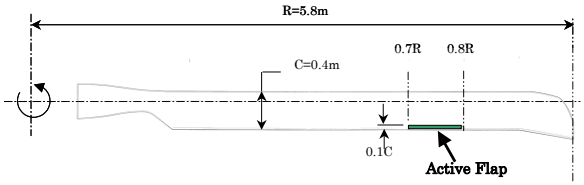

(a) Baseline blade with active flap

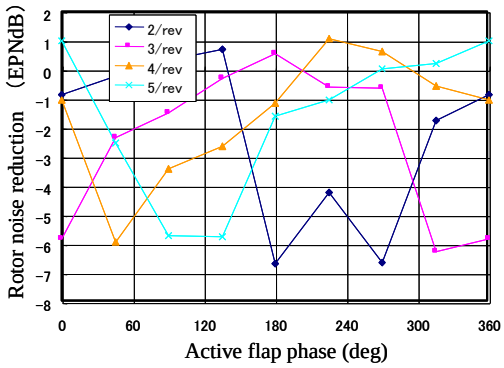

(b) Capability of BVI noise reduction by active flap

Figure 1. JAXA quiet rotor characteristics.

On the other hand, the analytical tool such as CFD technique has also developed in JAXA to investigate the more presice understanding about the flow field around a rotor and validate the noise reduction capability of JAXA quiet rotor blade[22, 23]. The flow field surrounding a helicopter is very complicated, being unsteady in nature and having numerous separation points due to its generally complex geometry. In addition, such flow field in question comprises a wide range of speeds, from almost zero to close to Mach 0.9 for example, when considering the speed difference between the rotor blade root and the blade tip. In order to be successfully applied to an entire helicopter configuration containing the main and tail rotors plus the fuselage, the computational scheme needs to be not only time accurate, but also to be able to handle the wide speed range that exists in helicopter flight. Several preconditioning methods are applied to this flow field and significant improvement in accuracy and convergence are reported[24, 25].

A newly developed CFD code in JAXA for full configured rotorcraft (named rFlow3D) adopts a modified version of the SLAU scheme (which stands for Simple Low-dissipative AUSM (Advection Upstream Splitting Method)[26]) conceived by Shima[27,28]. This scheme adjusts the numerical dissipation according to the local Mach number of the flow and is a kind of locally preconditioned scheme. Even without further preconditioning treatment to the implicit solver terms, the adoption of this scheme allows negation of the undesired effects of numerical dissipation that cause unrealistic divergence of the drag coefficient at very low mach numbers, thus improving the accuracy of the calculation of the flow field that comprises a wide range of velocity, from almost zero to transonic and supersonic. It is easy to construct an all speed CFD solver from a general compressible flow solver based on this approach where only the new numerical flux is used while other traditional solving procedures are kept unchanged. To investigate the blade elastic property, JAXA has developed the mode analysis code (called rMode) based on the Holtzer-Myklestad method and applied to the JAXA quiet rotor blade to obtain the natural frequency and elastic mode. The result showed a good correlation with those of CAMRAD II.

To reduce the vibration and/or noise of a helicopter, the adaptive controller[29] based on the transfer matrix was applied to the active devices such as active tab[30, 31] and active flap. In case of active tab, the closed loop controller has shown good capability to reduce the BVI noise. This controller also apllied to the active flap to reduce the vibration reduction of the vertical load of a helicopter in this paper. The results will be shown later.

2. JAXA Quiet rotor

2.1 Rotor description [21,32, 33]

The JAXA quiet rotor (called as JLNB) has four articulated blades, with a radius of 5.8 m and a nominal chord of 0.4 m. The baseline tip speed is 200 m/sec. Figure 1 shows the blade planform. The AT2 tip shape and AK airfoil contours are based on ATIC research (ref. [34]). Table 1 gives the rotor parameters. The hinge offset is 5.7% R.

Table 1. JAXA quiet rotor parameters.

radius, R	5.8	m
chord, c	0.4	m
number of blades	4	
flap and lag hinge offset	330	mm
solidity, $\sigma = Nc/\pi R$	0.0878	
torque offset	18	mm
pitch link radial station	330	mm
pitch link offset (forward of pitch axis)	180	mm
nominal twist	–10	deg
pitch link stiffness	TBD	
lag damper	TBD	
flap and lag hinge spring	55000	N-mm/deg
pitch bearing spring	15000	N-mm/deg
Lock number	4.9	
trailing edge flap		
radial extent	70-80	% R
edge gap	2	mm
chord	10	% c
hinge (no gap)	90	% c
airfoils		
$r = 0$ to 80% R	AK120G	
r =80%R to tip	AK100G	

2.2 Active flap

Figure 2 illustrates the full-scale onboard active flap system design, which was sized based on the results of ref.[32]. The flap span is 10% R and the flap chord is 10% c. Two piezo actuators operate in an out-of-phase reciprocated mode in the directions of compression and extension. The displacements of the actuators are augmented by an integrated one-piece amplifying mechanism that generates linear reciprocating movement and transmits this driving force to a push-pull linkage by an elastic hinge. The geometrical amplifying index,

which is the ratio between the displacement of the tip of the amplifying mechanism and that of actuator, is 10. Finally, the active flap is driven by the linkage through a composite hinge installed between the trailing edge of the blade and the leading edge of the flap. These design features are adopted to suppress free play in the drive mechanism to obtain the target amplitude by the least actuation power.

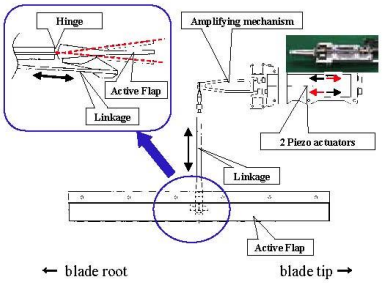

(a) Schematic of active flap system.

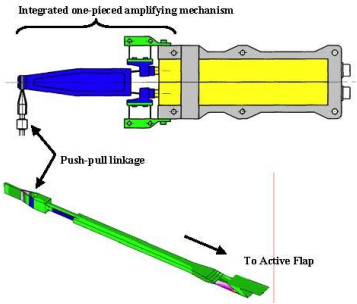

(b) Integrated one-piece amplifying mechanism and push-pull linkage.

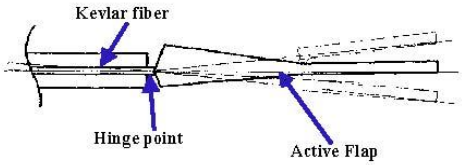

(c) Hinge portion of active flap.

Figure 2. Full-scale onboard active flap system..

2.3 Aerodynamic characteristics of airfoil by flap

The 2D wind tunnel test for the AK100 and AK120 airfoil with active flap has been conducted in the JAXA 2D transonic wind tunnel in order to obtain the 2D aerodynamic effect of flap[35,36]. In figure 3 and 4, the typical aerodynamics for two airfoils are shown. AK100 and AK120 airfoil was designed by Kawasaki Heavy Industries for ATIC project.

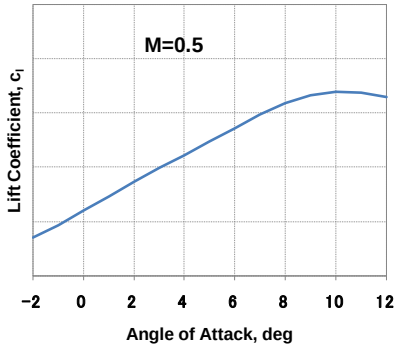

(a) Lift curve

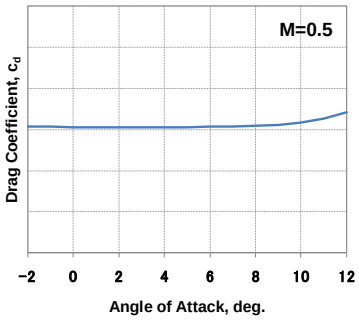

(b) Darg curve

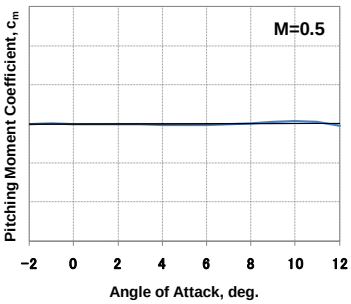

(c) Pitching moment curve

Figure 3. Aerodynamic property of AK100 airfoil at M=0.5 without flap.

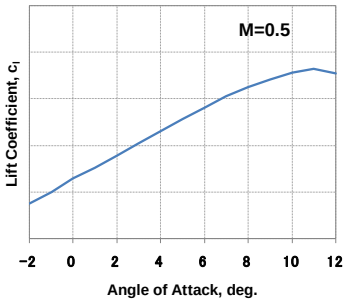

(a) Lift Curve

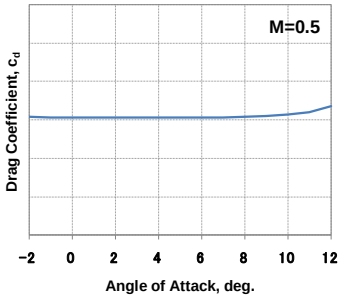

(b) Drag curve

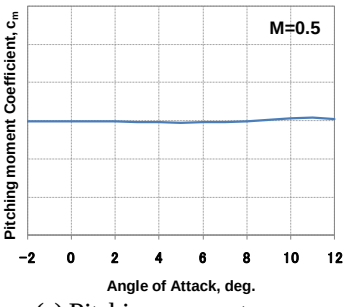

(c) Pitching moment curve

Figure 4. Aerodynamic property of AK120 airfoil at M=0.5 without flap.

Figure 5 shows the effect of the flap angle on aerodynamics of AK120GT airfoil at M=0.5.. Flap angle is defined as positive when flap is down. It is clear that the lift

and pitching moment are strongly affected by flap angle. This pitching moment change may be used to deform the pitch angle of blade elastically.

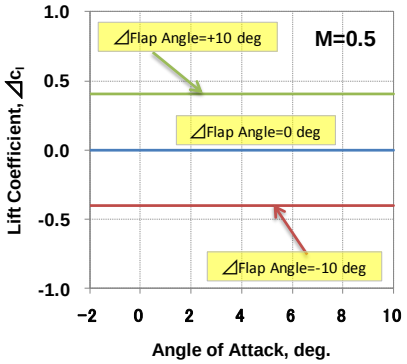

(a) Lift curve

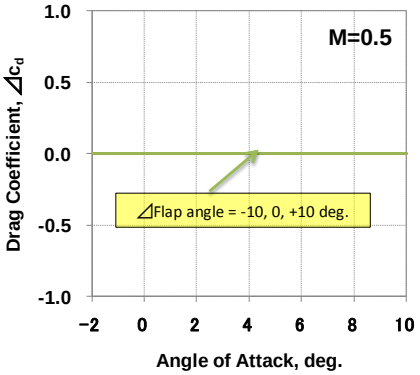

(b) Drag curve

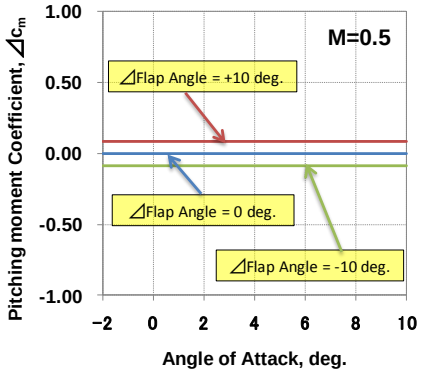

(c) Pitching moment curve

Figure 5. The effect of flap deflection on aerodynamics of AK120GT airfoil at M=0.5.

3. Analytical Tools

3.1 Complihensive code: <L MT/L CM>

3.1.1 Fundamental theory[37-39]

Professor A. Azuma and his colleagues of his laboratory have developed the aerodynamic analytical tools for helicopter in the 1970's [37]. These tools are based on the combination of the momentum theory and blade element theory. Compared with other aerodynamic tools such as vortex theory, this tool needs more short computing time to calculate the rotor aerodynamic and dynamic properties of helicopters.

In the Local Momentum Theory (LMT), the induced velocities at each blade spanwise position have been determined by means of the instantaneous momentum balance at specified spanwise position. The basic theory is described below. First of all, an elliptical wing has an elliptical lift distribution as shown in figure 6. The induced velocity distributed on the elliptical wing is constant as v_0. This value is half compared with the velocity at the infinite distance. It is supposed that the arbitrary wing is decomposed by the N elliptical wings (Fig.7). In this figure, (a) shows the symmetrical arrangement and (b) shows the one-sided arrangement. Supposed that the lift is L_i and constant induced velocity is Δv of the *i*-th wing, then total lift of this wing become as follows.

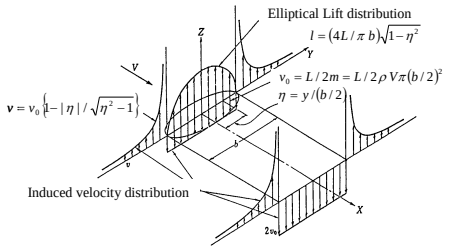

Figure 6. Airloading and induced velocity distribution of an elliptical wing.

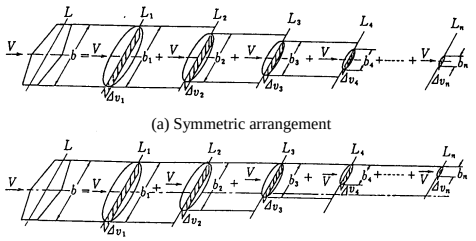

(a) Symmetric arrangement

(b) one-sided arrangement

Figure 7. Decomposition a straight wing to an elliptical wing.

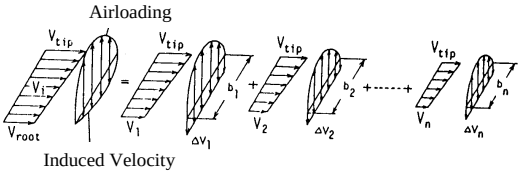

Figure 8. Decomposition of a rotary wing to wings having elliptical circulation distribution

$$L = \sum_{i=1}^{N} L_i = \sum_{i=1}^{N} 2\rho\pi(b_i/2)^2 V\Delta v_i \qquad (2\text{-}1)$$

Let think about the symmetrical arrangement of an arbitrary wing. If the upwash of the *i*-th elliptical wing can be ignored, then a lift and an induced velocity can be obtained at the arbitrary elliptical wing as follows respectively.

$$l_j = \sum_{i=1}^{j} l_i(\xi) = \sum_{i=1}^{j} (4L_i/\pi b_i)\sqrt{1-\xi^2} \qquad (2\text{-}2)$$

$$v_j = \sum_{i=1}^{j} \Delta v_i$$

where $\xi = y/(b_i/2) = \eta(b/b_i)$, b is span length of an arbitrary wing. To determine the induced velocity, Δv_j, of the *j*-th elliptical wing, the lift at the local position $(-\eta_i, -\eta_{i-1})$ has to balance between the lift generated by the blade element theory and the lift by local momentum as follows.

$$l_i = \int_{-\eta_j}^{-\eta_{j+1}} (1/2)\rho V^2 c_j a\left\{\theta_j - \sum_{i=1}^{j}(\Delta v_i/V)\right\}(d\eta/\Delta\eta_j) \qquad (2\text{-}3)$$

$$= \sum_{i=1}^{j} 2\overline{m_i}\Delta v_i$$

where,

$$\Delta\eta_j = \eta_j - \eta_{J+1}$$

$$\overline{m_i} = \int_{-\eta_j}^{-\eta_{j+1}} \rho b_i V\sqrt{1-(b/b_i)^2\eta^2}\,(d\eta/\Delta\eta_j)$$

$$c_j = c\left[1-(\eta_j+\eta_{j+1})/2\right]$$
$$\theta_j = \theta\left[1-(\eta_j+\eta_{j+1})/2\right] \tag{2-4}$$

$c_j, \theta_j, \overline{m_i}$ are a chord, pitch angle, mass of the flow passing through the circle with the diameter based on the span length of the *i*-th wing of the *j*-th ellipsoidal wing, ρ, a are air density and 2D lift slope of the wing section. The *j*-th induced velocity of the *j*-th elliptical wing, can be obtained in the Eq. (2-2). In the case of the one-sided arrangement, the same procedure can be applied in order to obtain the induced velocity.

To apply this method to the rotary wing, a rotating blade is decomposed in to N elliptical wings as shown in figure 8. (Strictly speaking, as a rotating blade is operating in the shear flow, the wing having elliptical lift distribution does not have elliptical wing shape. However the elliptical wing shape is supposed in this method,). Each decomposed elliptical wing is distributed in the one-sided arrangement. In the arrangement, the mass passing through the *i*-th elliptical wing at the position of (x_i, R, R) is obtained in the following equation.

$$m_i = \rho S_i V_{i,c}$$
$$= \rho\pi\left\{R(1-x_i)/2\right\}^2\left\{V\sin\varphi + R\Omega(1+x_i)/2\right\} \tag{2-5}$$

where,

$$x = \left\{(1+x_i)+\xi(1-x_i)\right\}/2$$

or

$$\xi = \left\{2x-(1+x_i)\right\}/(1-x_i)$$

At *x* span position, lift can be obtained with the same way of fixed wing case as follows.

$$l_i = \int_{x_i}^{x_{i+1}} (1/2)\rho V_i^2 c_i a(\theta_i-\phi_i)(dx/\Delta x_i)$$
$$= \int_{x_i}^{x_{i+1}} \sum_{i'}^{i}\left[4L_{i'}/\{\pi R(1-x_i)\}\right]$$
$$\times\left[\left\{R\Omega x + V\sin\left(\varphi_{k,0}+\sum_{\lambda=1}^{j-1}\Delta\varphi_\lambda\right)\right\}\right] \tag{2-6}$$
$$\times\sqrt{1-\left\{(2x-1-x_{i'})/(1-x_{i'})\right\}^2}\,(dx/\Delta x_i)$$

where,

$$\Delta x_i = x_{i+1}-x_i$$
$$V_i = V\sin\left(\varphi_{k,0}+\sum_{\lambda=1}^{j-1}\Delta\varphi_\lambda\right)+R\Omega\left\{(x_i+x_{i+1})/2\right\}$$
$$c_i = c\left[x=(x_i+x_{i+1})/2\right]$$
$$\theta_i = \theta\left[x=(x_i+x_{i+1})/2\right] \tag{2-7}$$
$$\phi_i = (V_N+v_{l,m}+v_{i,j,k})/V_i$$
$$V_N = V\sin(i_s)$$
$$L_i = 2\rho S_i V_{i,c}\left(v_{i,j,k}-v_{i-1,j,k}\right)$$

where $\varphi_{k,0}$ and $\Delta\varphi$ are the initial value of the azimuth angle and step value for the *k*-th blade. Horizontal speed V_i, θ_i and ϕ_i are function of azimuth angle, therefore each parameter has subscript of *j* and *k*. However in the above equation, such subscript is omitted for abbreviation. Subscript if *i*, *j* and *k* means the spanwise position, time or azimuth angle and *k*-th blade respectively.

Once the induced velocity can be obtained using above procedure, a lift distribution along a blade span can be obtained. However the helicopter blade encounters the induced velocity generated by a preceding blade. To realize the phenomena, the mesh is introduced in the calculation as shown in figure 9. At the local mesh (l', m'), the induced velocity for each blade remains at every time step. This process is explained in figure 10.

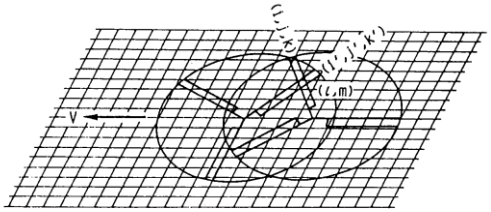

Figure 9. Representation of the successive impulse of a local station in the rotor plane of an advancing rotor.

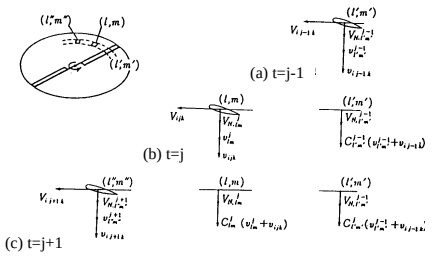

Figure 10. Successive change of the induced velocity in the rotational plane of a rotor.

At $t = j-1$, let suppose that a blade element proceeds with speed $V_{i,j,k}$. The vertical velocity has three components as vertical component of forward speed, V_N, induced velocity generated by the blade itself, $V_{i,j-1,k}$ and resultant induced velocity generated by preceding and own blade, $v_{l',m'}^{j-1}$. At mesh positions (l,m) and (l'',m''), at which a blade pass through at time $t=t$ and $t=t+1$ respectively, induced velocity still remains. However the magnitude of induced velocity maintains no more the same values. The attenuation coefficient, *C*, will introduce in order to estimate the decay rate of the induced velocity as shown in figure 10. This coefficient, *C*, is the function of span position, azimuth angle, namely time. At time, $t = j$, the induced velocity is defined as

$$v_{lm}^{j} = C_{lm}^{j-1}\left(v_{lm}^{j-1}+\sum_{i=1}^{N}\sum_{k=1}^{B} v_{i,j-1,k}\delta_{lm}\right) \tag{2-8}$$

where *B* is the number of blades. The definition of this attenuation coefficient is explained in ref .[38] in detail.

The LMT was applied to the windmill aerodynamics with some modification. This new method is referred to as "Local circulation method (LCM). The main modification is described as follows. Each blade element is expressed by the bound vortex and induced velocity at 25% chordwise position is decided by assumption that local flow at 75% chordwise position pass through along the wing. This method is described in ref.[39].

These two analytical tools were applied to the various phenomena in order to investigate the aerodynamic properties of the helicopter rotors and windmill, propeller, advanced turbo prop propeller etc.

3.1.2 Application of LMT and LCM

The Local Momentum Theory has been applied to investigate

the dynamic response of a single rotor helicopter[40,41] ans also othe type of helicopters, for example tandem rotor[42] and co-axial rotor[43], wind turbine[44] and advanced turbprop propeller such as counter-rotating propeller[45, 46]. Also to investigation of the effect of trailing tip vortex generated from a large-scaled airplane such as Jumbo jet airplane on helicopter, this complihensive code has developed and studied the dynamic response of a helicopter[47].

3.2CFD code

3.2.1 Governing Equations: < rFlow3D>[23]

The flow solver used to compute the flow field is based on the Euler equations discretized with the finite volume method. Because the rotor blade is moving and deforming, an Arbitrary Lagrangian-Eulerian (ALE) formulation[48] is used. The governing equations are

$$\frac{\partial}{\partial t}\int_{V(t)}\mathbf{U}dV+\int_{S(t)}\mathbf{F}\cdot\mathbf{n}dS=0 \tag{3-1}$$

where,

$$\mathbf{U}=\begin{pmatrix}\rho\\ \rho\mathbf{v}\\ \rho e\end{pmatrix} \tag{3-2}$$

is the conservative variables vector and

$$\mathbf{F}=\begin{pmatrix}(\mathbf{v}-\dot{\mathbf{x}})\cdot\mathbf{n}\rho\\ (\mathbf{v}-\dot{\mathbf{x}})\cdot\mathbf{n}\rho\mathbf{v}+p\mathbf{n}\\ (\mathbf{v}-\dot{\mathbf{x}})\cdot\mathbf{n}\rho e+p\mathbf{v}\cdot\mathbf{n}\end{pmatrix}=\widehat{\mathbf{F}}-\mathbf{U}\dot{\mathbf{x}} \tag{3-3}$$

is the physical flux vector. Here $V(t)$ is the moving control volume and $S(t)$ is the boundary surface surrounding the volume and $\mathbf{n}$ is the normal vector to the surface pointing outward from the control volume, where

$$\mathbf{v}=\begin{pmatrix}u\\ v\\ w\end{pmatrix} \tag{3-4}$$

is the velocity of the flow, and

$$\dot{\mathbf{x}}=\begin{pmatrix}\dot{x}\\ \dot{y}\\ \dot{z}\end{pmatrix} \tag{3-5}$$

is the velocity of the moving grid.

Here ρ is density, p is pressure, and e is the specific total energy. For a perfect gas, $P=(\gamma-1)\rho(e-\frac{1}{2}\mathbf{v}\cdot\mathbf{v})$ is the state equation of gas, and for air, the ratio of specific heats is $\gamma=1.4$. The sonic speed *c* is obtained as $c=\sqrt{\gamma(p/\rho)}$.

3.2.2 Discretization with Finite-Volume-Method (FVM)

Applying the Finite-Volume-Method to Eq.(3-6), considering the averaged value of **U** inside the control volume V, we have

$$\frac{\partial(V\mathbf{U})}{\partial t}+\mathbf{R}=0 \tag{3-6}$$

with

$$\mathbf{R}=\int_{S(t)}\mathbf{F}\cdot\mathbf{n}dS \tag{3-7}$$

At cell *i*, a family of two-levels implicit scheme for Eq.(3-6) can be obtained as:

$$\frac{V_i^{n+1}\mathbf{U}_i^{n+1}-V_i^n\mathbf{U}_i^n}{\Delta t}+(1-\alpha)\mathbf{R}_i^{n+1}+\alpha\mathbf{R}_i^n=0 \tag{3-8}$$

where n is time level and when $\alpha=0$, Eq.(3-8) is the backward Euler method with 1st order in time. When $\alpha=\frac{1}{2}$, it becomes a Crank-Nicolson method with 2nd order in time.

$$\mathbf{R}_i=\sum_{j\in N(i)}\tilde{\mathbf{F}}_{ij}s_{ij} \tag{3-9}$$

is a discretized form of **R** in Eq.(3-7), where $N(i)$ means the neighbor cells of cell *i*, and $\tilde{\mathbf{F}}_{\mathrm{y}}$ is the numerical flux from cell *i* to cell *j* and s_{ij} is the area interfacing cell *i* and cell *j*.

3.2.3 GCL (Geometry Conservation Law) Satisfaction

To satisfy the Geometry Conservation Law (GCL), a common grid velocity for face S_{ij} between time step *n* to *n+1* can be defined as

$$(v_n)_{ij}^{n+1/2}=[\dot{\mathbf{x}}\cdot\mathbf{n}]_{ij}^{n+1/2}=\left(\frac{V_i^{n+1}-V_i^n}{\Delta t}\right)_j\Big/\left((1-\alpha)s_{ij}^{\,n+1}+\alpha s_{ij}^{\,n}\right)=\frac{\Delta V_{ij}^{n+1/2}}{\Delta t\left((1-\alpha)s_{ij}^{\,n+1}+\alpha s_{ij}^{\,n}\right)} \tag{3-10}$$

where $\Delta V_{ij}^{n+1/2}$ is the swept volume by face S_{ij} from time level *n* to time level *n+1*. It must be noted that α is included in Eq.(3-10).

3.2.4 Dual time stepping [49]

Eq.(3-8) represents a nonlinear system of coupled equations, that has to be solved at each time step. It can be solved by treating it as a steady-state problem by introducing a pseudo-time variable τ so that

$$V^{n+1}\frac{\partial\mathbf{U}}{\partial\tau}+\mathbf{R}_*(\mathbf{U})=0 \tag{3-11}$$

where

$$\mathbf{R}_*(\mathbf{U})=\frac{V^{n+1}\mathbf{U}}{\Delta t}+(1-\alpha)\mathbf{R}(\mathbf{U})+\alpha\mathbf{R}^n-\frac{V^n\mathbf{U}^n}{\Delta t} \tag{3-12}$$

If Eq.(3-11) converged, then Eq.(3-8) is satisfied and **U** can be taken as $\mathbf{U}^{n-1}$ which has time accuracy as defined in Eq.(3-8).

3.2.5 Original LU-SGS Method

For the solution of Eq.(3-11), using backward Euler time integration, it can be written as

$$V^{n+1}\frac{\Delta\mathbf{U}^m}{\Delta\tau}+\mathbf{R}_*(\mathbf{U}^{m+1})=0 \tag{3-13}$$

where $\Delta\tau$ is the pseudo-time increment, m is the pseudo-time step, and

$$\Delta\mathbf{U}^m=\mathbf{U}^{m+1}-\mathbf{U}^m \tag{3-14}$$

Eq.(3-13) can be linearized in time by setting

$$\mathbf{R}_*(\mathbf{U}^{m+1})=\mathbf{R}_*(\mathbf{U}^{m+1})+\frac{\partial\mathbf{R}_*{}^m}{\partial\mathbf{U}}\Delta\mathbf{U}^m \tag{3-15}$$

this yields

$$\left[\frac{V^{n+1}}{1-\alpha}\left(\frac{1}{\Delta\tau}+\frac{1}{\Delta t}\right)I+\frac{\partial\mathbf{R}^m}{\partial\mathbf{U}}\right]\Delta\mathbf{U}^m=-\mathbf{R}^m-\frac{V^{n+1}\mathbf{U}}{(1-\alpha)\Delta t}+\frac{1}{1-\alpha}\left(\frac{V^n\mathbf{U}^n}{\Delta t}-\alpha\mathbf{R}^n\right) \tag{3-16}$$

or

$$\left[\frac{V^{n+1}}{1-\alpha}\left(\frac{1}{\Delta\tau}+\frac{1}{\Delta t}\right)I+\frac{\partial\mathbf{R}^m}{\partial\mathbf{U}}\right]\Delta\mathbf{U}^m=\mathbf{Res}^m \tag{3-17}$$

Following the original LU-SGS[49] approach, **R** in the left-hand side is reduced to spatially 1st- order as

$$\tilde{\tilde{\mathbf{F}}}_{\mathrm{ij}}=\frac{1}{2}\left[\mathbf{F}_i+\mathbf{F}_j-\lambda_{ij}(\mathbf{U}_j-\mathbf{U}_i)\right] \tag{3-18}$$

so that,

$$\bar{\mathbf{R}}_i=\sum_{j\in N(i)}\tilde{\tilde{\mathbf{F}}}_{\mathrm{ij}}s_{ij}=\sum_{j\in N(i)}\frac{1}{2}\left[\mathbf{F}(\mathbf{U}_i,\mathbf{n}_{ij})+\mathbf{F}(\mathbf{U}_j,\mathbf{n}_{ij})-\lambda_{ij}(\mathbf{U}_j-\mathbf{U}_i)\right]s_{ij} \tag{3-19}$$

The spectral radius is

$$\lambda_{ij}=\left|\left(\mathbf{v}_{ij}-\dot{\mathbf{x}}_{ij}\right)\cdot\mathbf{n}_{ij}\right|+c_{ij}=\left|\mathbf{v}_{ij}\cdot\mathbf{n}_{ij}-(v_n)_{ij}\right|+c_{ij} \tag{3-20}$$

Solving steps for Eq.(3-17) are

step 1: Calculate $\mathbf{D}_i$

$$\mathbf{D}_i = \left(\frac{V_i^{n+1}}{1-\alpha} \left(\frac{1}{\Delta\tau} + \frac{1}{\Delta t} \right) + \frac{1}{2} \sum_{j \in N(i)} \lambda_{ij} s_{ij} \right) \mathbf{I} \tag{3-21}$$

step 2: Forward sweep

$$\mathbf{D}_i \Delta\mathbf{U}_i^{(*)} = \mathbf{Res}_i^{(m)} - 0.5 \sum_{j \in L(i)} \left\{ \left[\mathbf{F}(\mathbf{U}_j^{(m)} + \Delta\mathbf{U}_j^{(*)}, \mathbf{n}_{ij}) - \mathbf{F}(\mathbf{U}_j^{(m)}, \mathbf{n}_{ij}) \right] - \lambda_{ij} \Delta\mathbf{U}_j^{(*)} \right\} s_{ij} \tag{3-22}$$

where $L(i)$ are the neighboring lower side cells

step 3: Backward sweep

$$\Delta\mathbf{U}_i^{(m)} = \Delta\mathbf{U}_i^{(*)} - \mathbf{0.5} \mathbf{D}_i^{-1} \sum_{j \in U(i)} \left\{ \left[\mathbf{F}(\mathbf{U}_j^{(m)} + \Delta\mathbf{U}_j^{(*)}, \mathbf{n}_{ij}) - \mathbf{F}(\mathbf{U}_j^{(m)}, \mathbf{n}_{ij}) \right] - \lambda_{ij} \Delta\mathbf{U}_j^{(*)} \right\} s_{ij} \tag{3-23}$$

where $U(i)$ are the neighboring upper side cells

step 4: Update $\mathbf{U}$

$$\mathbf{U}_i^{(m+1)} = \mathbf{U}_i^{(m)} + \Delta\mathbf{U}_i^{(m)} \tag{3-24}$$

when $m = 0$: $\mathbf{U}^{(m)} = \mathbf{U}^n$; and $m = \mathbf{N_{sweep}}$: $\mathbf{U}^{(m+1)} = \mathbf{U}^{\mathbf{n+1}}$.

Repeat steps 1~4 in the pseudo-time for $\mathbf{N}_{\text{sweep}}$ times to obtain $\mathbf{U}^{n-1}$.

3.2.6 DP-LUR Method

For an efficient parallel computing, it is desirable to use the neighbor cell values only. A Data-Parallel Lower-Upper Relaxation (DP-LUR) Method[50] is utilized for each pseudo-time step:

$$\Delta\mathbf{U}_i^{[0]} = \mathbf{D}_i^{-1} \mathbf{Res}_i^{(m)} \tag{3-25}$$

$$\Delta\mathbf{U}_i^{[k]} = \mathbf{D}_i^{-1} \left\{ \mathbf{Res}_i^{(m)} - 0.5 \sum_{j \in N(i)} \left\{ \left[\mathbf{F}(\mathbf{U}_j^{(m)} + \Delta\mathbf{U}_j^{[k-1]}, \mathbf{n}_{ij}) - \mathbf{F}(\mathbf{U}_j^{(m)}, \mathbf{n}_{ij}) \right] - \lambda_{ij} \Delta\mathbf{U}_j^{[k-1]} \right\} s_{ij} \right\}$$

repeat Eq.(3-25) k_{max} times so that

$$\Delta\mathbf{U}_i^{(m)} = \Delta\mathbf{U}_i^{[k_{max}]}. \tag{3-26}$$

3.2.7 Modified SLAU Scheme for Numerical Flux

There are many schemes to obtain the numerical flux in Eq.(3-9). In the AUSM (Advection Upstream Splitting Method)–type scheme[26],

$$\tilde{\mathbf{F}} = \frac{\dot{m} + |\dot{m}|}{2} \mathbf{\Phi}^L + \frac{\dot{m} - |\dot{m}|}{2} \mathbf{\Phi}^R + \tilde{p}\mathbf{N} \tag{3-27}$$

Original SLAU scheme[27, 28] is extended to a moving grid as

$$\mathbf{\Phi} = \begin{pmatrix} 1 \\ u \\ v \\ w \\ h \end{pmatrix} \quad \text{and} \quad \mathbf{N} = \begin{pmatrix} 0 \\ x_n \\ y_n \\ z_n \\ v_n \end{pmatrix} \tag{3-28}$$

$$h = (e + p)/\rho \tag{3-29}$$

v_n calculated with Eq.(3-10) must be used to satisfy the GCL.

$$\tilde{p} = \frac{p^L + p^R}{2} + \frac{\beta^+ - \beta^-}{2}(p^L - p^R) + (1-\chi)(\beta^+ + \beta^- - 1)\frac{p^L + p^R}{2}$$

$$\beta^{\pm} = \begin{cases} \frac{1}{4}\left(2 \mp M^{\pm}\right)\left(M^{\pm} \pm 1\right)^2, & |M^{\pm}| < 1 \\ \frac{1}{2}\left(1 + sign(\pm M^{\pm})\right), & \mathbf{otherw} \end{cases}$$

$$M^+ = \frac{V_n^L - v_n}{\bar{c}}$$

$$M^- = \frac{V_n^R - v_n}{\bar{c}}$$

$$\chi = (1 - \hat{M})^2$$

$$\hat{M} = \min\left(1.0, \frac{1}{\bar{c}} \sqrt{\frac{(V_n^L - v_n)^2 + (V_n^R - v_n)^2}{2}}\right)$$

$$\dot{m} = \frac{1}{2}\left\{ \rho^L \left(V_n^L + |V_n|_{\max}^+ \right) + \rho^R \left(V_n^R - |V_n|_{\max}^- \right) - \frac{\chi}{\bar{c}} \Delta p \right\}$$

$$|V_n|_{\max}^{\pm} = (1-g)|V_n|_{\max} + g|V_n|^{\pm}$$

$$g = -\max(\min(M^+, 0), -1) \cdot \min(\max(M^-, 0), 1)$$

$$|V_n|_{\max} = \max(|V_n|^+, |V_n|^-) \tag{3-30}$$

$$\Delta p = p^R - p^L$$

$$\bar{c} = \frac{1}{2}\left(c^L + c^R\right)$$

here the speed normal to the face is calculated as

$$V_n = x_n u + y_n v + z_n w. \tag{3-31}$$

$\hat{M}$ in Eq.(3-30) is modified from the original form[26] to use the perpendicular velocity component instead of the local total speed at the cell face. In ref.[27], it was pointed out that this might cause instability in the calculations. But with the variables reconstructed with limiters (see next section), no instability was observed from the authors' experience. $\dot{m}$ in Eq.(3-30) is more natural and memory saving while applied to a moving grid system.

The SHUS scheme[51] that was applied until recently[52] had some shortcomings, as its numerical dissipation caused unrealistic diversion of its computational results at very low Mach numbers. A two-dimensional drag computation of the NACA 0012 airfoil as shown in figure 11 indicates that the results with the SHUS scheme tend to diverge at Mach numbers lower than 0.1. The SLAU scheme, by contrast, gave realistic drag coefficient values even at very low speeds under Mach 0.01, as well as those at high speed close to, and over Mach 1.

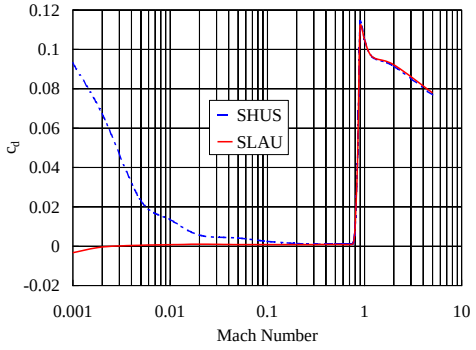

Figure 11. Drag vs. Mach Number for NACA 0012 Airfoil

The favorable characteristic of this computational scheme is considered to be well suited to the challenging demands of predicting the flow field surrounding helicopters where a wide range of air speed co-exists.

3.2.8 FCMT for Data Reconstruction

To improve the spatial resolution while keeping the favorable TVD (Total Variations Diminishing) property of the original scheme, a Fourth-order Compact MUSCL TVD (FCMT) interpolation method[53] is used to obtain the L (Left) and R (Right) values at the interfacing face with

$$q^L_{i+1/2} = q_i + \frac{1}{6}\left(\Delta^* \bar{q}_{i-1/2} + 2\Delta^* \tilde{q}_{i+1/2}\right)$$
$$q^R_{i+1/2} = q_{i+1} - \frac{1}{6}\left(2\Delta^* \bar{q}_{i+1/2} + \Delta^* \tilde{q}_{i+3/2}\right) \quad (3\text{-}32)$$

where,

$$\Delta^* \bar{q}_{i-1/2} = \mathrm{minmod}\left[\Delta^* q_{i-1/2}, b\Delta^* q_{i+1/2}\right]$$
$$\Delta^* \bar{q}_{i+1/2} = \mathrm{minmod}\left[\Delta^* q_{i+1/2}, b\Delta^* q_{i+3/2}\right]$$
$$\Delta^* \tilde{q}_{i+1/2} = \mathrm{minmod}\left[\Delta^* q_{i+1/2}, b\Delta^* q_{i-1/2}\right]$$
$$\Delta^* \tilde{q}_{i+3/2} = \mathrm{minmod}\left[\Delta^* q_{i+3/2}, b\Delta^* q_{i+1/2}\right] \quad (3\text{-}33)$$

and,

$$\Delta \bar{q}_{i-1/2} = \mathrm{minmod}\left[\Delta q_{i-1/2}, b_1\Delta q_{i+1/2}, b_1\Delta q_{i+3/2}\right]$$
$$\Delta \bar{q}_{i+1/2} = \mathrm{minmod}\left[\Delta q_{i+1/2}, b_1\Delta q_{i+3/2}, b_1\Delta q_{i-1/2}\right] \quad (3\text{-}34)$$
$$\Delta \bar{q}_{i+3/2} = \mathrm{minmod}\left[\Delta q_{i+3/2}, b_1\Delta q_{i-1/2}, b_1\Delta q_{i+1/2}\right]$$

and,

$$\Delta^* q_{i+1/2} = \Delta q_{i+1/2} - \frac{1}{6}\Delta^3 \bar{q}_{i+1/2}$$

$$\Delta^3 \bar{q}_{i+1/2} = \Delta \bar{q}_{i-1/2} - 2\Delta \bar{q}_{i+1/2} + \Delta \bar{q}_{i+3/2} \quad (3\text{-}35)$$

and,

$$\Delta \bar{q}_{i-1/2} = \mathrm{minmod}\left[\Delta q_{i-1/2}, b_1\Delta q_{i+1/2}, b_1\Delta q_{i+3/2}\right]$$
$$\Delta \bar{q}_{i+1/2} = \mathrm{minmod}\left[\Delta q_{i+1/2}, b_1\Delta q_{i+3/2}, b_1\Delta q_{i-1/2}\right] \quad (3\text{-}36)$$
$$\Delta \bar{q}_{i+3/2} = \mathrm{minmod}\left[\Delta q_{i+3/2}, b_1\Delta q_{i-1/2}, b_1\Delta q_{i+1/2}\right]$$

here,

$$\Delta q_{i+1/2} = q_{i+1} - q_i \quad (3\text{-}37)$$

In present calculations, $b = 4$, and $b_1 = 2$ is used.

3.2.9 Validation and Application of rFlow3D

rFlow3D has a potential to capture the more precise flow field around the helicopter. So far, this code has been applied to the rotor/fuselage interference problem[54-59]. To validate the accuracy of this code, the comparison between calculated results and experiments has been performed. In JAXA, in-house aerodynamic database about the JMRTS, shown in Figure 12, has been established and used for validation of this code[60].

Figure12. JMRTS(JAXA Multi-purpose Rotor Test System)

4. Aerodynamic Property

4.1 Mode Analysis: <rMode>[61,62]

In JAXA, the mode analysis code based on the beam theory, rMode, has been developed. The aerodynamic blade deformations such as flapping, torsion, and lead-lag deformations are calculated at each time step in CFD calculation. These deformations are calculated by using mode decomposition method. Mode calculation was performed by using the Myklestad method[63-65]. In this method, a blade is composed of several discrete masses and bays. Each bay has structural properties such as flapping bending stiffness, EI_y and the chordwise bending stiffness, EI_z and torsional stiffness, GJ. The blade torsional, flap bending, and chordwise bending equations of equilibrium can be derived respectively as follows:

$$\begin{aligned}
&-[(GJ + Tk_A^2)\phi']' + (EI_z - EI_y)\left[(w''^2 - v''^2)\frac{\sin 2\theta}{2} + v''w''\cos 2\theta\right] \\
&+ mk^2(\ddot{\phi} + \Omega^2\phi) + me[\ddot{w} - \theta\ddot{v} + \theta\Omega^2 v + e\Omega^2\phi + r\Omega^2(w' - \theta v')] \\
&= M_{ax} - m[eg + k^2(\ddot{\theta} + \Omega^2\theta + 2\Omega\theta\dot{v}')] + e\theta(e_0\Omega^2 - 2\Omega\dot{u})] \\
&\left[\{EI_y + (EI_z - EI_y)\sin^2\theta\}w'' + (EI_z - EI_y)\left(\frac{v''\sin 2\theta}{2} + \phi v''\cos 2\theta + \phi w''\sin 2\theta\right)\right]'' \\
&- (Tw')' + m(\ddot{w} + e\ddot{\phi}) \\
&= F_{az} - m(g + e\ddot{\theta} - e\Omega^2\theta) \\
&\left[\{EI_z + (EI_z - EI_y)\sin^2\theta\}v'' + (EI_z - EI_y)\left(\frac{w''\sin 2\theta}{2} - \phi v''\sin 2\theta + \phi w''\cos 2\theta\right)\right]'' \\
&- (Tv')' + m[\ddot{v} - e\theta\ddot{\phi} - \Omega^2(v - e\theta\phi)] \\
&= F_{ay} + m[-2\Omega\dot{u} + 2e\Omega(\dot{v}' + \theta\dot{w}') + e\theta\ddot{\theta} + \Omega^2(e_0 + 2e)]
\end{aligned} \quad (4\text{-}1)$$

When the coupled mode shapes and the associated frequencies are denoted by $\bar{w}$, $\bar{v}$, $\bar{\phi}$ and ω_j, respectively, blade deformations can be expressed as

$$w = \sum_{j=1}^{\infty} \bar{w}_j \cdot q_j, \quad v = \sum_{j=1}^{\infty} \bar{v}_j \cdot q_j, \quad \phi = \sum_{j=1}^{\infty} \bar{\phi}_j \cdot q_j \quad (4\text{-}2)$$

Where q_j is the generalize coordinate of the j^{th} coupled mode. According to the Rayleigh-Ritz approach[66], Eq. (4-1) result in the following form where the orthogonality condition of the natural modes was used in the derivation.

$$M_j\left\{\frac{d^2 q_j}{dt^2} + \omega_j^2 \cdot q_j\right\} = Q_j \quad (j = 1,2,3\cdots) \quad (4\text{-}3)$$

Where M_j and Q_j are a generalized mass and generalized force respectively shows as follows:

$$\begin{aligned}
M_j &= \int_0^R [(k^2\bar{\phi}_j + e\bar{w}_j - e\theta\bar{v}_j)\bar{\phi}_j + (\bar{w}_j + e\bar{\phi}_j)\bar{w}_j + (\bar{v}_j - e\theta\bar{\phi}_j)\bar{v}_j]mdr \\
Q_j &= \int_0^R [\{M_{ax} - m[eg + k^2(\ddot{\theta} + \Omega^2\theta + 2\Omega\theta\dot{v}') + e\theta(e_0\Omega^2 - 2\Omega\dot{u})]\}\bar{\phi}_j \\
&+ \{F_{az} - m(g + e\ddot{\theta} - e\Omega^2\theta)\}\bar{w}_j + \{F_{ay} + m[-2\Omega\dot{u} + 2e\Omega(\dot{v}' + \theta\dot{w}') \\
&+ e\theta\ddot{\theta} + \Omega^2(e_0 + 2e)]\} \times \bar{v}_j]dr
\end{aligned} \quad (4\text{-}4)$$

The radial extension of the blade u is approximated as

$$\begin{aligned}
u &= r - \int_0^r [1 + v'^2 + w'^2]^{\frac{1}{2}} dr \cong -\frac{1}{2}\int_0^r [v'^2 + w'^2]dr \\
&= \sum_{j=1}^{\infty} \bar{u}_j \cdot q_j
\end{aligned} \quad (4\text{-}5)$$

where

$$u = -\int_0^r w_0' \bar{w}_j' dr \quad (4\text{-}6)$$

w_0 = trim value of w

In order to take into the account of preconing angle β_0 of a blade, the aerodynamic forces and moments are change as follows:

For the flapwise correction:

$$F_{a,z} \Rightarrow F_{a,z} - \bar{m}_j r_j \Omega^2 \cos(\beta_0)\sin(\beta_0)$$

For the torsional correction:

$$M_{a,x} \Rightarrow M_{a,x} - F_{a,z} e_{EA} - e_{CG} \bar{m}_j r_j \Omega^2 \cos(\beta_0)\sin(\beta_0)$$

Where $F_{a,z}$, $M_{a,x}$ are the normal aerodynamics force and pitching moment respectively. Also $e_{EA,}$ e_{CG} are the distance between elastic axis and aerodynamics center (quarter chord) (Positive toward leading edge) and between elastic axis and center of gravity (positive toward leading edge). The inertial forces by these dynamic motions have not considered yet in the present flow solver.

To obtain a periodic solution for Eq.(4-3) per rotor revolution as required in the loose CFD/CSD coupling approach, the 2nd time derivative of q_j is written as

$$\frac{d^2 q_j}{dt^2} = \Omega^2 \frac{d^2 q_j}{d\Psi^2} \tag{4-7}$$

The 2nd azimuth-wise derivative is then approximated with a central difference expression,

$$\frac{d^2 q_j}{d\Psi^2} = \frac{q_{j,i+1} - 2q_{j,i} + q_{j,i-1}}{\Delta\Psi^2} \tag{4-8}$$

So by solving a cyclic tri-diagonal matrix system

$$\mathbf{Ax} = \mathbf{d}$$

$$\mathbf{A} = \begin{bmatrix} b_1 & c_1 & 0\ldots & a_1 \\ a_2 & b_2 & c_2 & 0\ldots \\ 0\ldots & .. & .. & .. \\ c_N & 0\ldots & a_N & b_N \end{bmatrix}, \ \mathbf{x} = \begin{bmatrix} q_{j,1} \\ q_{j,2} \\ \ldots \\ q_{j,N} \end{bmatrix}, \ \mathbf{d} = \begin{bmatrix} d_1 \\ d_2 \\ \ldots \\ d_N \end{bmatrix} \tag{4-9}$$

$$a_i = 1, \ b_i = \Delta\Psi^2 p_j^2 - 2, \ c_i = 1$$

$$d_i = \Delta\Psi^2 \Xi_{j,i}$$

the generalized amplitudes for each natural modes can be obtained without time-marching solutions.

In order to include the effect of the spring and/or damper at the rotor hub, the boundary condition at the blade root should be modified as follows:

$$(1)\ M_Y - w' \cdot SP_w = 0.0$$
$$(2)\ M_z - v' \cdot SP_v = 0.0$$
$$(3)\ M_x + \phi \cdot SP_\phi = 0.0$$

where SP_w, SP_v, SP_ϕ are spring constant for flapwise, dierction, chordwise direction, torsional direction respectively.

Figure 13 shows a fan plot for the JAXA real-size quiet rotor blade. JAXA results show good correlation with other computational results by NASA and KHI. Form this fugure, at the operation condition, the frequency of 1st torsional mode (18.094Hz) is very close to the 3/rev rotor frequency (16.46Hz) or 4/rev rotor frequency (21.95Hz) shown in table 2. This means that the toraionl response is sensitive to the excitinf force by active device such as a active flap or a active tab, etc. In this investigation, the active flap is installed to JLNB at the spanwaise postion between 70% to 89%. This active flap model has been applied the LMT to obtain the effect of the active flap on the elastic balde deflection of JLNB. Figure 14 shows the torsional response of the JLNB at the tip positon, in which the exciting frequency of active flap is 2/rev and the amplitude is ±6deg.. In the LMT calculation, up to 10 modes are used in present study to obtain the approximate deformations from Eq. (4-1). The calculation result shows that the range of torsional deflection is within -2 degree to 0.2 degree. The design target of the torsional deflection in order to reduce the BVI noise should be located within ±6 deg in the design condition. This is very satisfactory results for JLNB.

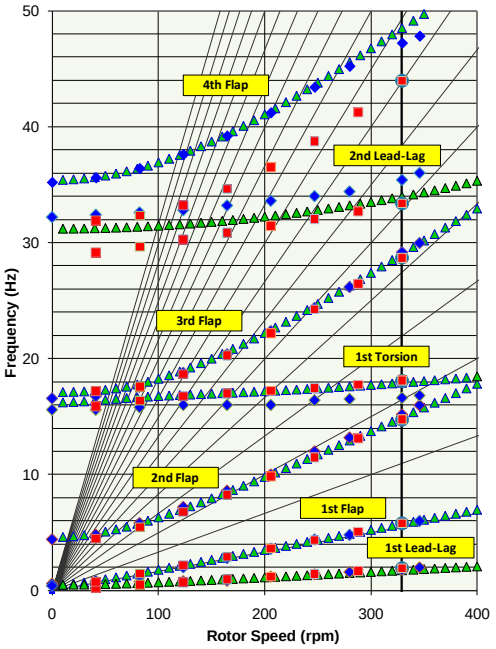

Figure 13. Fan plot of the JAXA Low Noise Blade (Legend : △: NASA, ◇:KHI, □: JAXA)

Table 2. Comparison of the natural frequency of JLNB wtih rotor revolution frequency

Mode	Natural Frequency	N x f_{blade}
1st Lead-Lag	1.9204	5.49
1st Flap	5.8041	10.98
2nd Flap	14.7475	16.46
1st Torsion	18.0941	21.95
3rd Flap	28.6832	27.44
2nd Lead-Lag	33.3968	32.93
4th Flap	43.9657	38.41

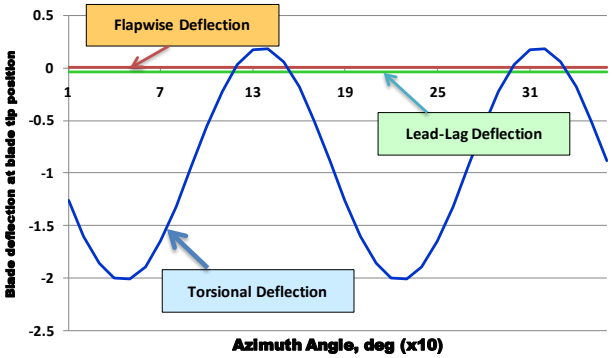

Figure 14. Torsional deflection at the tip position of JLNB

4.2 CFD-CSD coupling code[67]

In the loose coupling CFD/CSD approach, periodicity of the structural deformations is assumed and the solution procedure as shown in Eq.(4-9) can be used. The CFD based aerodynamic forces and moments are saved into a CFD to CSD data file per designated azimuth angles. In this study, every 10 degrees forces data are saved and after a longer than 360/NBLD rotation, an updated CFD-based forces distribution over whole revolution can be obtained. To eliminate the initial aerodynamic disturbance just after the new trim and blade deformations are applied, half revolution CFD

computation is carried out before each loose CFD/CSD iteration.

The loose CFD/CSD approach in present study is essentially same to the so-called delta methodology as proposed by AFDD[68] shown in figure 15. But it is drastically simplified by following assumptions so that the CSD code is compact enough to be directly integrated into the JAXA_ov3d CFD code[69].

(1) In the CSD trim adjustment computation, only the direct control changes are taken into account for the aerodynamic forces.
(2) Uniform inflow is assumed and based on the target trim thrust only, so it is constant during the whole computation.

Through above assumption combined with periodic deformation solution with Eq.(4-9), a simple and efficient integrated loose CFD/CSD approach is constructed. After the trim adjustment computation converges, the forces used in the CSD routines will be solely from the CFD results.

Trim adjustment is made by solve following equations:

$$\begin{bmatrix} \Delta\theta_0 \\ \Delta\theta_C \\ \Delta\theta_S \end{bmatrix} = \begin{bmatrix} \frac{\partial T}{\partial \theta_0} & \frac{\partial T}{\partial \theta_C} & \frac{\partial T}{\partial \theta_S} \\ \frac{\partial Mx}{\partial \theta_0} & \frac{\partial Mx}{\partial \theta_C} & \frac{\partial Mx}{\partial \theta_S} \\ \frac{\partial My}{\partial \theta_0} & \frac{\partial My}{\partial \theta_C} & \frac{\partial My}{\partial \theta_S} \end{bmatrix}^{-1} \begin{bmatrix} \Delta T \\ \Delta Mx \\ \Delta My \end{bmatrix} \tag{4-10}$$

where,

$$\begin{aligned} \Delta T &= T_{TARGET} - \left(T_{CFD} + T_{BET} - T_{BET,0}\right) \\ \Delta Mx &= Mx_{TARGET} - \left(Mx_{CFD} + Mx_{BET} - Mx_{BET,0}\right) \\ \Delta My &= My_{TARGET} - \left(My_{CFD} + My_{BET} - My_{BET,0}\right) \end{aligned} \tag{4-11}$$

The derivatives in Eq.(4-10) is estimated at each iteration numerically.

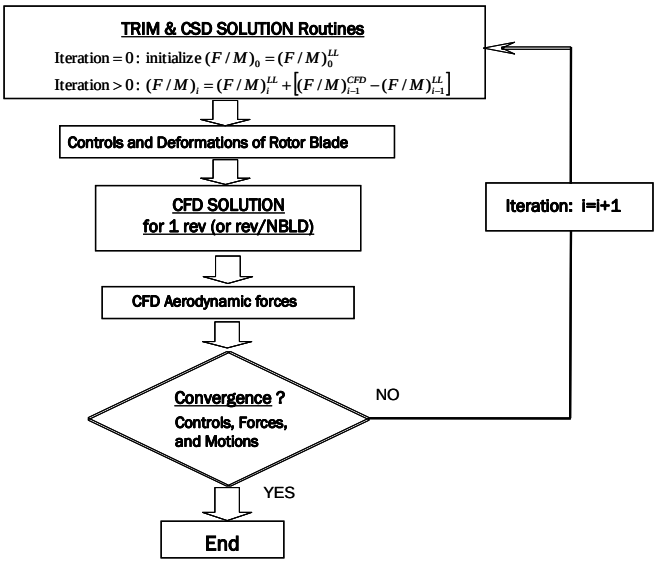

Figure 15. Loose coupling algorithm

4.3 Adaptive Control Theory[70]

4.3.1 Optimal Control Theory

In this study, the adaptive control algorithm is applied to reduce the acoustic property and noise property of a rotor. The control argorithm is based on the determination of a performance index, J that is a quadratic function of the input and output variables. Quadratic performance function to be used in this investigation is as follows:

$$J = Z_n^T W_z Z_n + \theta_n^T W_\theta \theta_n + \Delta\theta_n^T W_{\Delta\theta} \Delta\theta_n \tag{4-12}$$

where,

Z_n: measurements $(= [Z_{noise}, Z_{vibration}]^T)$ (4-13)
W_Z : weighting matrix for Z
θ_n : control input representing Active Flap frequency, amplitude and phase
W_θ : weighting matrix for θ
$\Delta\theta_n$: the difference of θ between successive control cycles
$W_{\Delta\theta}$: weighting matrix for $\Delta\theta_n$

W_Z, W_θ and $W_{\Delta\theta}$ are assumed to be diagonal and the same value for all harmonics of a particular quantity. For the measurements Z_n includes the noise measuremnts, Z_{noise} and vibration measurement, $Z_{vibration}$. To specify the measurement Z_n, the following two model are proposed to express the relationship bewteen control inputs and measuremets[70].

For global model:

$$Z_n = Z_0 + T\theta_n \tag{4-14}$$

For Local model:

$$\Delta Z_n = T\Delta\theta_n \tag{4-15}$$

where, ΔZ_n means $(Z_n - Z_{n-1})$ and $\Delta\theta_n$ means $(\theta_n - \theta_{n-1})$. For the deterministic controller, the control required to reduce the noise and vibration is given by substituting for Z_n in the performance function, J, using the helicopter model, and then solving for θ_n that minimizes J. For the global model in Eq. (4-14), the solution can be obtained as follows:

$$\theta_n = CZ_0 + C_{\Delta\theta}\theta_{n-1} \tag{4-16}$$

where,

$C = -DT^T W_z$
$C_{\Delta\theta} = DW_{\Delta\theta}$
$D = (T^T W_z T + W_\theta + W_{\Delta\theta})^{-1}$

For the local model in Eq.(4-15), the solution can be obtained as follows:

$$\theta_n = CZ_{n-1} + (C_{\Delta\theta} - CT)\theta_{n-1} \tag{4-17}$$

In this derivation, the response Z is assumed to be deterministic; therefore, it is refered to as the deterministic controller. When the parameter uncertainties are taken into account, the cautious controller can be obtained by using the expected value of the performance function:

$$\begin{aligned} J &= E(Z_n^T W_z Z_n) + \theta_n^T W_\theta \theta_n + \Delta\theta_n^T W_{\Delta\theta} \Delta\theta_n \\ &= E\left[\sum_j w_{zj} z_{jn}^2\right] + \theta_n^T W_\theta \theta_n + \Delta\theta_n^T W_{\Delta\theta} \Delta\theta_n \end{aligned} \tag{4-18}$$

where it is assumed that w_z is diagonal, and θ_n remains deterministic. $E(\,)$ means the expectation of $(\,)$. For the case of the open-loop controller (z_0 feedback), there follows:

$$\begin{aligned} E\left[\sum_j w_{zj} z_{jn}^2\right] &= E\sum_j \left[w_{zj}\left(z_{j0} + \theta_n^T t_{jn}\right)^2\right] \\ &= \sum_j w_{zj}\left(\hat{z}_{j0} + \theta_n^T t_{jn}\right)^2 \\ &\quad + \sum_j w_{zj}\left(M_{zz} + 2\theta_n^T + \theta_n^T M_{tt}\theta_n\right) \end{aligned} \tag{4-19}$$

where,

$$M = \begin{bmatrix} M_{tt} & M_{tz} \\ M_{zt} & M_{zz} \end{bmatrix}$$

$M_{tt} = (\text{n x m})$ matrix

$M_{tz} = M_{zt}^{T}$ vector

$M_{zz} =$ scalar

So the performance function becomes

$$J = Z_n^T W_z Z_n + \theta_n^T W_\theta \theta_n + \left(\theta_n^T, 1\right)\left(\sum_j w_{zj} M_{jn}\right)\begin{pmatrix}\theta_n \\ 1\end{pmatrix} + \Delta\theta_n^T W_{\Delta\theta}\Delta\theta_n \quad (4\text{-}20)$$

For the solution of this controller that minimizes J is then

$$\theta_n = CZ_0 + C_{\Delta\theta}\theta_{n-1} + C_0 \quad (4\text{-}19)$$

where the gain matrices C and $C_{\Delta\theta}$ are the same as for the deterministic controller, using the identified values of the parameters and with W_θ replaced by

$$W_\theta + \left[\sum_j w_{zj}(M_{tt})_{jn}\right] \quad (4\text{-}22)$$

The new constant term is

$$C_0 = -D\left[\sum_j w_{zj}(M_{tz})_{jn}\right] \quad (4\text{-}23)$$

Similarly, for the case of the closed-loop controller (Z_{n-1} feedback), the performance function is

$$J = Z_n^T W_z Z_n + \theta_n^T W_\theta \theta_n + \Delta\theta_n^T\left(W_{\Delta\theta} + \sum_j w_{zj} M_{jn}\right)\Delta\theta_n \quad (4\text{-}24)$$

The solution is identical to that for the deterministic controller, using the identified values of the parameters, and with $W_{\Delta\theta}$ replaced by

$$W_{\Delta\theta} + \sum_j w_{zj} M_{jn} \quad (4\text{-}25)$$

4.3.2 Regulator

A controller combined recursive parameter estimation and kinear feedback is called a self-tuning regulator. There are two fundamental options for the identification: the use of either an invariable algorithm or an adaptive algorithm. There are also two fundamental options for the controller: open-loop or closed-loop. Hence, there are four possible regulator configurations. For the adaptive algorithm, the parameters are recursively identified on-line, using a Kalman filter. For the open-loop algorithm, the control is based on the uncontrolled vibration level Z_0 (identified either on-line or off-line). For the closed-loop algorithm, the control is based on the feedback of the measured vibration, Z_{n-1}.

4.5 Noise Prediction Method: <rNoise>[71]

The prediction method of the far field acoustic pressure is based on the combination of CFD technique with an acoustic equation solver. Although direct computation can be used to get the noise solution directly from the flow calculation with CFD based methods, this is available only in the near field in spite of huge computing cost. At present, the best way is the coupling with the integral method for far-field prediction. Acoustic analogy[71], which is re-arranged into the Ffowcs Williams-Hawkings equation, is widely used and still under construction for better applications. Retarded time solution to this equation, neglecting quadruple noise, can be written in the form of Formulation 1 by Farassat[72,73].

The prediction of rotor noise is conducted in the following procedures:

1) calculation of sound pressure of the noise source,
2) acoustic prediction computation at the observer position, and
3) post-processing of the noise data in the way of sound level using visualization or audible converting.

Hypothesis of the Ffowcs-Williams and Hawkings equation[74] to be satisfied are known that the noise source must lay in low speed flow, and the observer should be located outside of the source region (i.e. outside of the boundary layer, separation flow or wake) in order to avoid the nonlinear effect. In most calculations to compare the results with experiment by wind tunnel, the observer moves in the same direction and at the same speed as the noise source. The pressure distribution on the blade surface calculated by the CFD code is stored every 0.5 degrees in azimuth-wise direction as the input data in noise calculation.

The acoustic pressure p, which is the function of an observer position x and an observer time t, satisfies the wave equation as follows:

$$\left(\frac{1}{c^2}\frac{\bar{\partial}^2 p}{\partial t^2} - \bar{\nabla}^2 p\right)\cdot H(f) = -\left(\hat{p}_n + \frac{1}{c}M_n\hat{p}_t\right)\delta(f) - \frac{1}{c}\frac{\bar{\partial}}{\partial t}\{M_n\hat{p}\delta(f)\} - \bar{\nabla}\cdot\{\hat{p}\boldsymbol{n}\delta(f)\} \quad (4\text{-}21)$$

where $H(f)$ is the Heaviside function and $\delta(f)$ is the Dirac delta function. The quantity c is the speed of sound. The bar over the operator symbol denotes operators involving generalized derivatives[75]. The vector n and, M_n, $\hat{p}$, $\hat{p}_n$ and p_t in Eq. (4-21) are described as follows:

$$\boldsymbol{n} = \nabla f$$

$$M_n = \frac{1}{c}\frac{\partial f}{\partial t}$$

$$\hat{p} = \lim_{f\to+0} p(\boldsymbol{x}, t) \quad (4\text{-}22)$$

$$\hat{p}_n = \nabla\hat{p}\cdot\nabla f,\ \hat{p}_t = \frac{\partial\hat{p}}{\partial t}.$$

By using the Green function in unbounded space, Eq.(4-21) gives

$$p(\boldsymbol{x},t)\cdot H(f) = \int_{-\infty}^{t} d\tau\int G^0\left\{-\left(\hat{p}_n + \frac{1}{c}M_n\hat{p}_t\right)\delta(f) - \frac{1}{c}\frac{\partial}{\partial t}[M_n\hat{p}\delta(f)] - \nabla\cdot[\hat{p}\boldsymbol{n}\delta(f)]\right\}d\boldsymbol{y} \quad (4\text{-}23)$$

where,

$$G^0(\boldsymbol{y},\tau\,|\,\boldsymbol{x},t) = \frac{1}{4\pi r}\delta(g), \quad (4\text{-}24)$$

and

$$g = \tau - t + \frac{r}{c}. \quad (4\text{-}25)$$

In Eq.(4-24), the vector $\boldsymbol{y}$ is a source position, $\boldsymbol{\tau}$ is a source time. In Eq.(4-25), r is the distance between a source and an observer position. By performing the integration on the influential surface in Eq.(4-23), the following equation is

obtained.

$$4\pi p(\boldsymbol{x},t)\cdot H(f)= -\int \frac{\hat{p}_n + M_n\hat{p}_t/c}{r\Lambda}d\Sigma + \int \frac{\hat{p}\cos\theta}{r^2\Lambda}d\Sigma + \frac{1}{c}\frac{\partial}{\partial t}\int \frac{(\cos\theta - M_n)\hat{p}}{r\Lambda}d\Sigma \quad (4\text{-}26)$$

where,

$$\Lambda = \sqrt{1 + M_n - 2M_n \cos\theta} \quad (4\text{-}27)$$

In Eq.(4-26), Σ is the influential surface generated by all Γ-curves as the source time τ varies $-\infty$ to t for the fixed observer position $\boldsymbol{x}$ and time t, where the Γ-curve is the intersection of body and sphere $g = 0$. The function g is defined by Eq.(4-25) and $g = 0$ shows the sphere on which the acoustic pressure transmits in the space. The quantity θ is the angle between $\boldsymbol{n}$ and $\boldsymbol{r}$ [74]. Figure 16 shows the schematic view of the influential surface. In the figure 17, the chart of the acoustic analysis used in this investigation is shown.

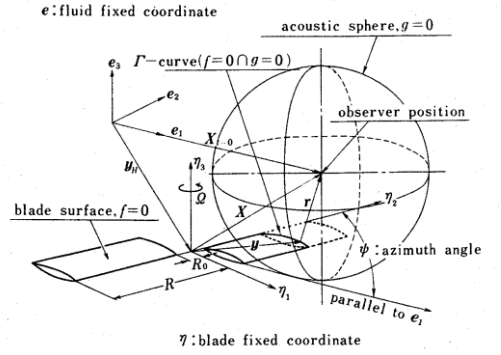

Figure 16. Schematic view of the influential surface.

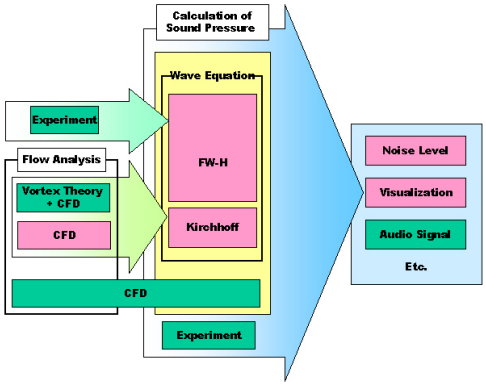

Figure 17. The chart of acoustic analysis.

5. Results and Discussions

5.1 Aerodynamic analysis

5.1.1 Aerodynamic Performance of JLNB at Hover

For the investigation of the aerodynamic performance of JLNB, hover aerodynamic calculation has been performed by using LMT and rFlow3D. Figure 18 shows the thrust performance at hover.

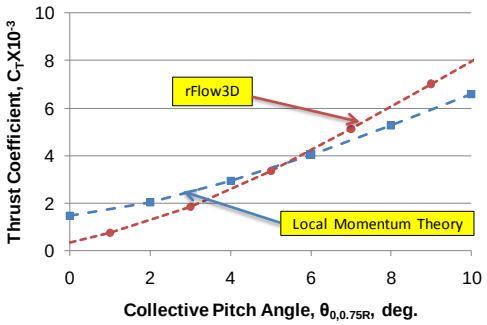

(a) Thrust vs. Collective pitch angle

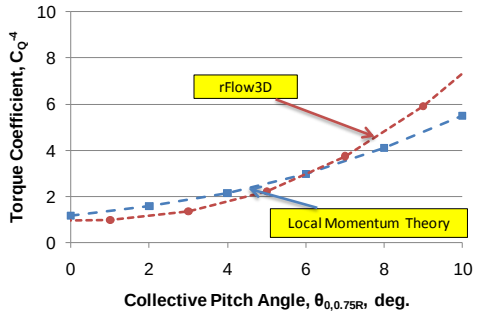

(b) Torque vs. Collective pitch angle

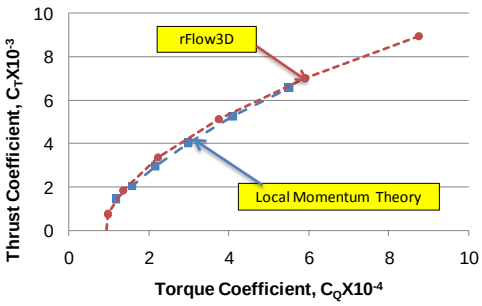

(c) Polar curve

Figure 18. Aerodynamic performance at Hover.

In figure 19, the vortex system around a JLNB rotor calculated by rFlow3D is shown. In this CFD calculation, a modified SLAU scheme is embedded to handle the all-speed of a flow around the rotor. In this figure, the vortices from the root region of the rotor are well captured. Tip vortices from the tip region are also well maintained under the rotor for one revolution. Though a coarse grid is used in this calculation, rFlow3D code shows the vortex capturing capability.

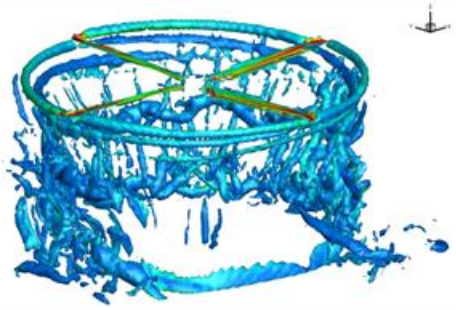

(a) Vortex generated from Blades by Q-criterion

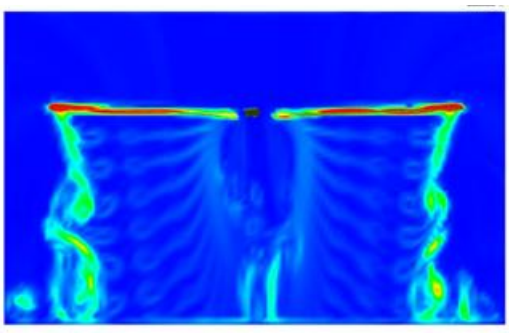

(b) Vortex property in vertical cross section

Figure 19. Vortex structure of NINJA rotor at hover.

5.1.2 Vibration Reduction by active flap

In this section, the effect of the active flap on the vibration reduction has been investigated theoretically. The adaptive controller which has described in the section 4.3.1 and 4.3.2 has been installed in the comprehensive code, LMT for the JLNB rotor. In this investigation, as measurements Z_n, the following form has been introduced.

$$Z_n = [C_{T4C}, C_{T4S}, C_{H4C}, C_{H4S}, C_{M4C}, C_{M4S}, C_{Y4C}, C_{Y4S}, C_{L4C}, C_{L4S}, -C_{Q4C}, -C_{Q4S}]^T \quad (4\text{-}26)$$

These values denotesthe 4/rev vibratory aerodynamic property of the rotor. The inputs of the controller is defined as follows:

$$\theta_n = [\theta_{f3C}, \theta_{f3S}, \theta_{f4C}, \theta_{f4S}, \theta_{f5C}, \theta_{f5S}] \quad (4\text{-}27)$$

where θ_{fNC}, θ_{fNS} are cosine and sine element of the pitch angle of active flap for N/rev frequency respectively. As the adaptive controller, the deterministic closed-loop algorithm was used in this investigation. Figure 20 shows the aerodynamic properties of JLNB rotor without control.

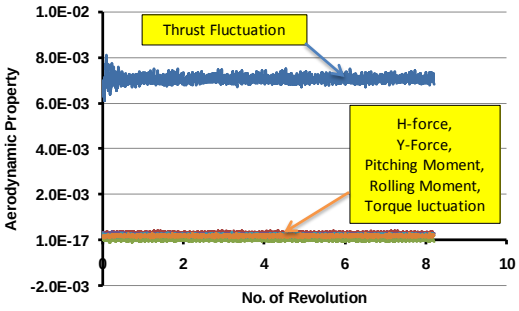

Figure 20. Aerodynamic property without control

The results applied the adaptive controller to JLNB are shown from figure 21 to figure 22. In figure 21, the thrust fluctuation shows little change compared with that of figure 20. On the contrary, the 1/rev to 6/rev fluctuation conponent of rotor thrust has been derived by using the FFT shown in Figure 23. All fluctuation conponents show the vibration reduction owing to the adaptive controller in figure 23. The adaptive controller showed good capability to reduce the vibratory level of the rotor thrust.

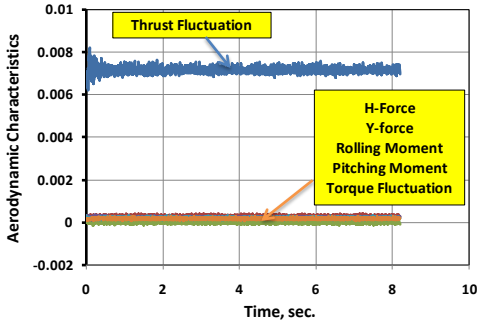

Figure 21. Aerodynamic property with control

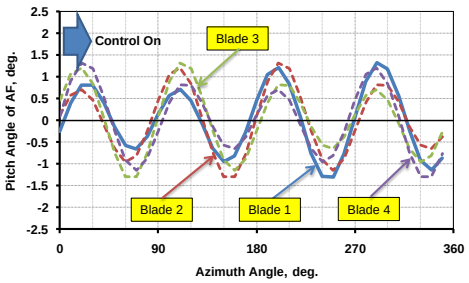

Figure 22. Active Flap angle for 4/rev vibration reduction

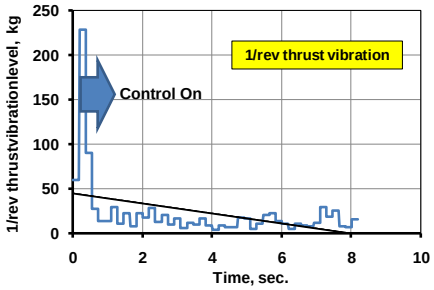

(a) 1/rev thrust vibration level

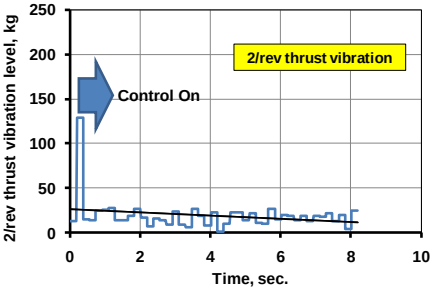

(b) 2/rev thrust vibration level

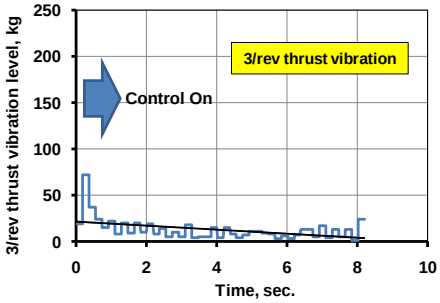

(c) 3/rev thrust vibration level

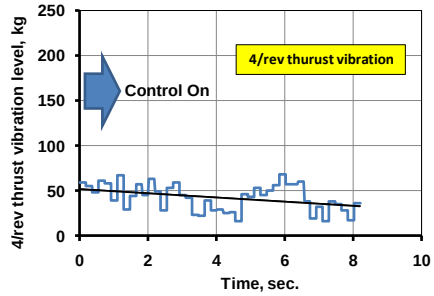

(d) 4/rev thrust vibration level

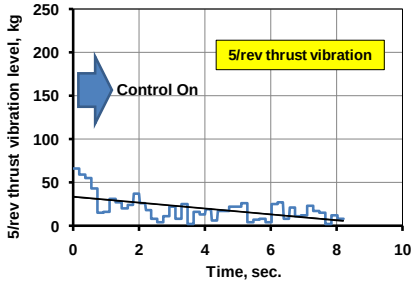

(e) 5/rev thrust vibration level

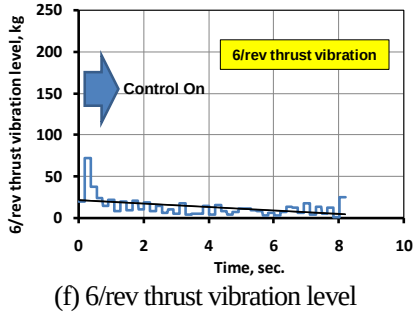

(f) 6/rev thrust vibration level

Figure 23. Thrust vibration reduction effect by Active Flap

5.2 Aeroacoustic analysis

5.2.1 Noise Reduction by active flap[30,31]

For the BVI noise reduction, the adptive optimal controller has been applied to the one-bladed model rotor in the wind tunnel. Figure 24 shows the rotor apparatus in the open secton wind tunnel. Three microphones were installed near the rotor apparatus to measure the BVI noise generated from the rotor. The main features of the active flap are also shown in Table 3.

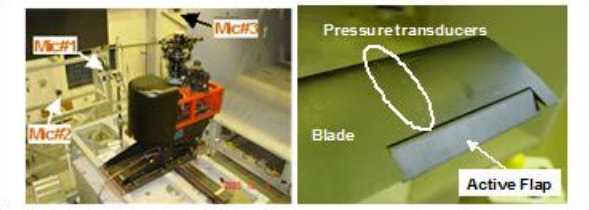

Figure 24. One-blade rotor apparatus in the open section wind tunnel and active flap installation.

Table 3. Features of rotor system and Active Flap

Hub type	rigid in flap and lead-lag
Rotor radius	1m
Blade chord	0.12m
Airfoil	NACA0012
Blade plan form	Rectangular
Rotor rpm	1200rpm (max)
Collective pitch	-5 to +15deg.
Cyclic pitch	0deg. (fixed)
Active Flap	Amp. : 30deg.(max)
	Freq. : 20Hz
	Phase : variable
	Chord : 25%c
	Span : 80 ~ 98%R

In this investigation, measurements of noise were specified by the pressure jump of the surface pressure on a blade as follows:

$$Z_{noise} = \Delta C_{p_{\max}} = \frac{\Delta Cp_{\max}(ch2) + \Delta Cp_{\max}(ch19) + \Delta Cp_{\max}(ch20)}{3}$$

The pressure transducers are embedded in the blade as shown in figure 25, except for the active flap portion because of difficulty for wiring between non-oscillating blade and oscillating active flap. The location of pressure transducer is also shown in this figure.

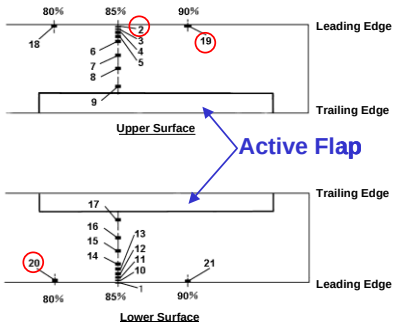

Figure 25. Pressure transducer distribution

The effect of active flap phase on $\Delta C_{p_{max}}$ measured at the blade leading edge is shown in figure 26 comparing with the sound pressure level. The correlation between the sound pressure level and $\Delta C_{p_{max}}$ with respect to active flap phase can be seen. Active flap phase range around 160 deg. simultaneously has the largest rotor noise reduction indicated by the sound pressure level and the maximum BVI relief effect represented by $\Delta C_{p_{max}}$. This characteristic of $\Delta C_{p_{max}}$ with respect to active flap phase is useful as an input to the control law, because the BVI can be detected and evaluated by only on-board sensors.

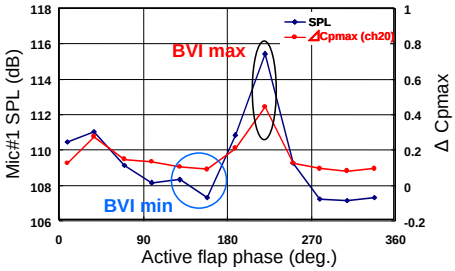

Figure 26. Correlation between ΔCpmax and SPL with respect to Active Flap phase by open-loop control.

Figure 27 shows the control system in the wind tunnel testing for evaluating the closed loop control law, which was conducted using a 1-bladed rotor system. The control inputs are usually defined as flap frequency, amplitude and phase angle. Because of the mechanical limitation that the rotor system can change only active flap phase automatically, the active flap phase only was used as inputs parameter in the closed loop control law.

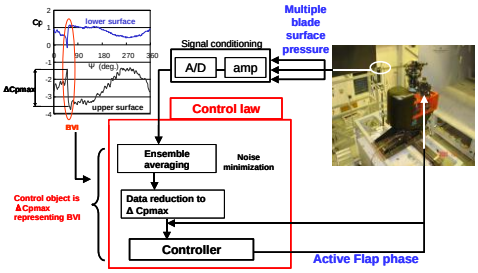

Figure 27. Control system in wind tunnel testing.

As control input, the following only phase angle was used as mentioned before.

$$\theta_n \equiv \begin{bmatrix} \cos\phi_{AF} \\ \sin\phi_{AF} \end{bmatrix}$$

where, ϕ_{AF} is the active flap phase.

Figure 28 shows the SPL level for measured SPL (Mic#1) and measured Z_{noise} for open-loop controller and the convergency of the controller for both SPL target and $\Delta C_{p_{max}}$ target for closed-loop controller. From this figure, it is clear shown that the measued SPL has the strong correlation with Z_{noise}. This means the pressure on a blade can be used as an index of controllerfor noise reduction.

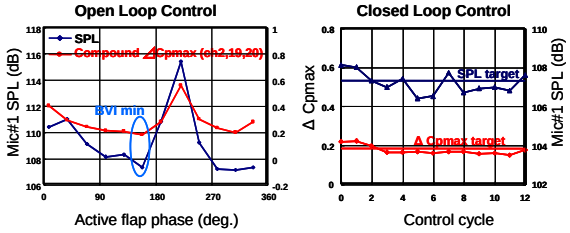

Figure 28. Wind tunnel test result of closed loop control with compound ΔCpmax

5.2.2 Noise reduction by activ flap for JLNB

JAXA active flap system is applied to the JLNB in order to investigate the effect on BVI noise reduction into the rFlow3D code. Figure 29 shows the grid system used in this analysis. The overlapped grid method is used, in which three grids are

involved, one is blade grid, the other is inner and outer back grid. Table 4 shows the grid points in forward flight.There are three spacing in the inner back grid. In this analysis, standard grid system (grid spacing of 0.1c, c:blade chord) is used in order to capture the presice tip vortex and BVI phenomena.

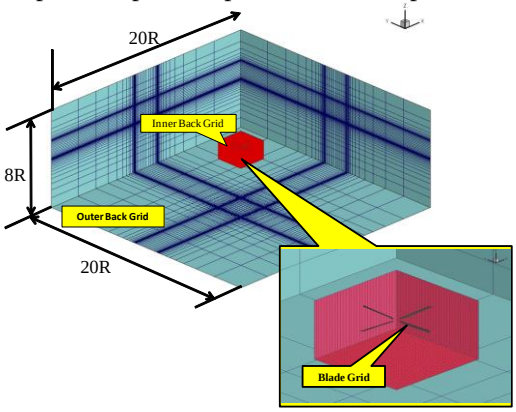

Figure 29. Grid system in rFlow3D

Table 4. Grid system in forward flight

Blade grid (span × chord × normal)	141 × 101 × 21
Inner back ground grid (X×Y×Z)	311 × 233 × 69 (coarse) 465 × 349 × 103 (standard) 619 × 465 × 137 (fine)
Outer back ground grid (X×Y×Z)	151 × 101 × 101
Spacing of Inner back grid size	0.15c (coarse) 0.10c (standard) 0.075c (fine)

In this analysis, the following flap control is considered.

$$\theta_f = A_f cos\,(\omega_f\, t - \phi_f)$$

where θ_f is the flap angle, A_f, t are the amplitude of flap angle and time, (ω_f, ϕ_f) are frequency and phase angle of active flap, respectively. In this calculation, an amplitude of $\pm$ 6 deg and frequency of 2/rev (2Ω) are selected. + sign of flap angle shows the downward direction. the elastic defromation is also included in the blade elasticity. The controller is open loop. Therefore only phase angle against rotor blade is consider inthe controller to reduce the noise in this analysis. The calculation condition is shown in Table 5.

Table 5. Calculation conditions

Items		unit
For Rotor		
Advance Ratio, μ	0.15	
Rotor Rotational Speed, Ω	34.48	rad/sec.
Rotor Radius, R	5.8	m
Blade Chord, c	0.4	m
Descending Angle, λ	5.3	deg.
For Flap		
Amplitude, A_f	6	deg.
Frequency, ω_f	68.96	rad/sec.
Phase, Φ_f	Variable	deg.

In figure 30, Q-criteiron Iso-surface plot was shown. In this figure, votex from a flap has been generated. It is clear that as the strength of vortex from a flap depends on the lift strength on the flap surface. In figure 31, this vortex changes the rotational direction alternately because of the pitch angle change. This vortex works to draw or seperate each other. This phenomena means the trajectory of the tip vprtex may be changed inward or outerward direction.

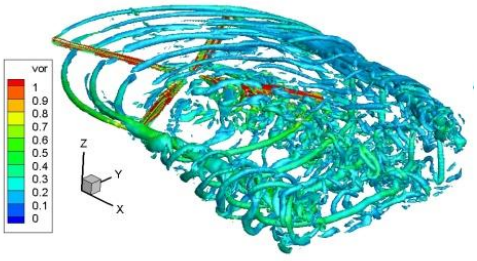

Figure 30. Q-criterion Iso-surface Plot for JLNB with Synthesized Blade Deformation, ($\mu = 0.15$)

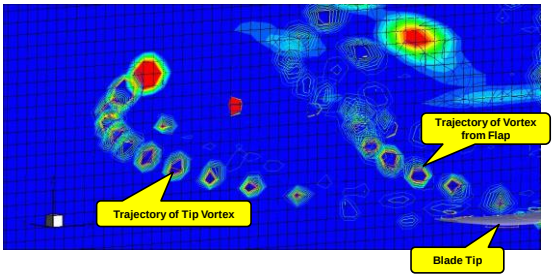

Figure 31. Trajectory of tip vortx and vortex from flap

In figure 32, noise carpet contour derived from the results of rFlow3D is shown for the baseline blade which means no flap activation. In the advancing side of a rotor, a region of high noise level (hot spot) is appeared. The maximun noise level reachs 117 dB in this case.

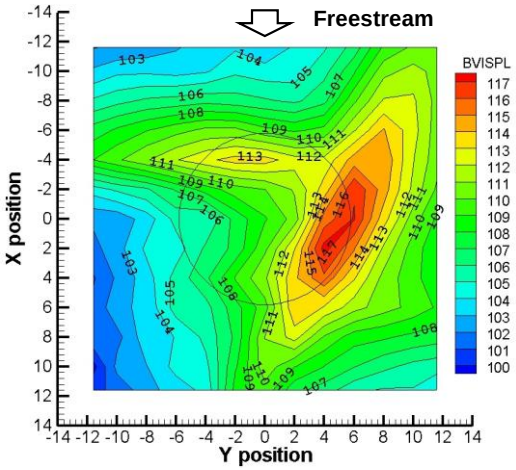

Figure 32. Noise carpet (BVISPL) for baseline blade. With no flap actuation.

To investigate the effect of an active flap on noise reduction, an active flap with several kinds of phase angle has been applied in this preliminary analysis. In these cases, an amplitude of an active flap is fixed at $\pm$6 deg. and only phase angle of an active flap has been changed from 0 deg. to 360 deg. In fugure 33, BVISPL of JLNB for phase angle of an active flap has compared with each others. The comparison was performed at the maximum point of the hot spot for balseline case. Even these analysis has compared the only one point, the global tendency is greatly similar with figure 26in the experiments[31]. From this figure, the phase angle of the minimum BVISPL will locate in between 90 deg. and 180 deg.

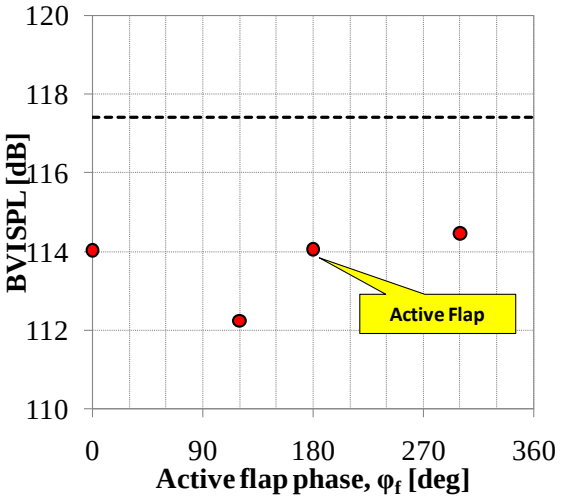

Figure 33. Comparison of BVISPL of JLNB for phase angle of an active flap.

6. Concluding Remarks

JAXA real-size quiet rotor system has been designed. Using the JAXA in-house code such as rMode, rFlow3D and rNoise, the aerodynamic and acoustic performance have been investigated. The effect of an active flap on the vibration and noise reduction by using the adaptive controller has also been investigated in this paper. The main results are drawn as follows:

- The high performance and low noise rotor blade with an active flap has been designed. To use the more soft torsional stiffness along span direction, it is easy to deform the blade torsionally. JAXA real-sized active flap has potential to achieve the $\pm$ 1.5 deg. torsional deflection at the blade tip.
- The natural frequencies obtained by rMode are good agrrement with those of CAMRAD II. From the analysis, 1st torsional frequency is very close to 3/rev. and 4/rev. frequencies of rotor.
- Concerning with the aerodynamic performance, analytical results using LMT and rFlow3D shows good correlation with each other.
- For the vibration reduction using an active flap, the adaptive controller has been used in the LMT. The results show that 1st to 6th Fourier expansion components of thrust were totally reduce by this adaptive control.
- The adaptive controller has been applied to the one-bladed rotor test stand to reduce the BVI noise. Even phase angle as control input is used in the wind tunnel test, the controller showed good performance for BVI Noise reduction.
- From the rFlow3D analysis, the usage of an active flap installed on a blade is very efective to reduce BVI noise in approach flight condition. From these preliminary calcualtions using open loop control (changing the phase angle of an active flap), about 5 dB BVI noise reduction at the 120 deg. phase angle of an active flap was shown.

In this paper, the preliminary wind tunnel test and calculations by rFlow3D for BVI noise reduction have been done using open/closed loop control. Even the results show the promising for not only noise reduction but also vibration reduction. It is necessary that more presice analysis should be performed in the future work.

7. References

[1] Shaw, J., Higher Harmonic Blade Pitch Control: A System for Helicopter Vibration Reduction. Doctor of Philosophy Thesis, Massachusetts Institute of Technology, 1980.

[2] Jacklin, S., Blaas, A.,Teves, D., Kube, R., 1995. Reduction of Helicopter BVI Noise, Vibration, and Power Consumption Through Individual Blade Control, American Helicopter Society 51st Annual Forum, Fort Worth, Texas, May 9-11.

[3] Jacklin, S., Haber, A., Simone, G., Norman, T., Kitaplioglu, C., Shinoda, P., 2002. Full-Scale Wind Tunnel Test of an Individual Blade Control System for a UH-60 Helicopter, American Helicopter 58th Society Annual Forum, Montréal, Canada, June 11-13.

[4] Hassan, A.A., Charles, B.D., Tadghighi, H. and Sankar, L.N., Blade-Mounted Trailing Edge Flap Control for BVI Noise Reduction. NASA CR 4426, February 1992.

[5] Chopra, I., Status of Application of Smart Structures Technology to Rotorcraft Systems, Journal of American Helicopter Society, Vol. 45, No. 4, pp. 228-252, 2000.

[6] Enenkl, B., Klöppel, V., Preißler, D., Full Scale Rotor with Piezoelectric Actuated Blade Flaps, 28th European Rotorcraft Forum, Bristol, United Kingdom, September 17-19, 2002.

[7] Hasegawa, Y., Katayama, N., Kobiki, N., Nakasato, E., Yamakawa, E., Okawa, H., Experimental and Analytical Results of Whirl Tower Test of ATIC Full Scale Rotor System, American Helicopter Society 57th Annual Forum, Washington D.C., May 9-11, 2001.

[8] Hasegawa, Y., Katayama, N., Kobiki, N., Yamakawa, E., Whirl Test Results of ATIC Full Scale Rotor System, 26th European Rotorcraft Forum, The Hague, The Netherlands, September, 2000.

[9] Weems, D. B., Anderson, D. M., Mathew, M. B., Bussom, R. C., A Large-Scale Active-Twist Rotor, American Helicopter Society 60th Annual Forum, Baltimore, MD, May, 2004.

[10] Wilbur, L., Mirick, H., Yeager, T., Langston, W., Cesnik, E., Shin, S., Vibratory Loads Reduction Testing of the NASA/Army/MIT Active Twist Rotor, Journal of American Helicopter Society, Vol.47, No.2, April, pp.123-133, 2002.

[11] Kobiki, N., Kondo, N., Saito, S., Akasaka, T., Tanabe, Y., Active Tab, a New Active Technique for Helicopter Noise Reduction, 29th European Rotorcraft Forum, Friedrichshafen, Germany, September 16-18, 2003.

[12] Kobiki, N., Akasaka, T., Kondo, N., Tanabe, Y., and Saito, S., An Experimental Study of On-blade Active Tab for Helicopter Noise Reduction, 30th European Rotorcraft Forum, Marseilles, France, September 14-16, 2004.

[13] Kobiki, N., Saito, S., Akasaka, T., Tanabe, Y., Fuse, H., An Experimental Study for Aerodynamic and Acoustic Effects of On-blade Active Tab, 31st European Rotorcraft Forum, Italy, September, 2005.

[14] JanakiRam, R.D, Sim, B.W., Kitapliglu, C. and Straub, F.K., Blade-Vortex Interaction Noise Characteristics of a Full-Scale Active Flap Rotor, American Helicopter Society 65th Annual Forum, Grapevine, Texas, May 27-29, 2009.

[15] Sim, B.W., JanakiRam, R.D., Barbely, N.L. and Solis, E., Reduced In-Plane Low frequency Noise of an Active Flap Rotor, American Helicopter Society 65th Annual Forum, Grapevine, Texas, May 27-29, 2009.

[16] Rauch, P., Gervais, M., Cranga, P., Baud, A., Hirsch, J-F., A. Walter, A. and Beaumier, P., BLUE EDGE™: The Design,

Development and Testing of a new blade Concept, American Helicopter Society 67th Annual Forum, Virginia Beach, USA, May 3-5, 2011.
[17] Dieterich, O., Enenkl, B., Roth, D., Trailing Edge Flaps for Active Rotor Control Aeroelastic Characteristics of the ADASYS Rotor System, American Helicopter Society 62nd Annual Forum, Phoenix, AZ, May 9-11, 2006.
[18] Jaenker, P., Hermle, F., Friedl, S., Lentner, K., Enenkl, B., Mueller, C., Advanced Piezoelectric servo Flap System for Rotor Active Control, 32nd European Rotorcraft Forum, Maastricht, The Netherlands, 2006.
[19] Roth, D., Enenkl, B., Dieterich, O., Active Rotor Control by Flaps for Vibration Reduction – Full scale demonstrator and first flight test results –, 32nd European Rotorcraft Forum, Maastricht, The Netherlands, 2006.
[20] Konstanzer, P., Enenkl, B., Aubourg, P.A. and Cranga, P., Recent advances in Eurocopter's passive and active vibration control, American Helicopter Society 64th Annual Forum, Montreal, Canada, April 2008.
[21] Kobiki, N., Saito, S., Fukami, T. and Komura, T., Design and Performance Evaluation of Full Scale On-Board Active Flap System. American Helicopter Society 63th Annual Forum, Virginia Beach, VA, May 2007.
[22] Ochi, A., Aoyama, T., Saito, S., Shima, E. and Yamakawa, E., BVI Noise Predictions by Moving Overlapped Grid Method, American Helicopter Society 55th Annual Forum, May 1999.
[23] Tanabe, Y., and Saito S., Significance of All-Speed Scheme in Application to Rotorcraft CFD Simulations, The 3rd International Basic Research Conference on Rotorcraft Technology, Nanjing, China, October 14-16, 2009.
[24] Renaud, T., O'Brian, D., Smith, M. & Potsdam, M., "Evaluation of Isolated Fuselage and Rotor-Fuselage Interaction Using Computational Fluid Dynamics," Journal of American Helicopter Society, Vol.53, No.1, pp.3-17, January 2008.
[25] Potsdam, M., Sankaran, V. & Pandya, S., Unsteady Low Mach Preconditioning with Application to Rotorcraft Flows, 18th AIAA CFD Conference, 25-28 June 2007, Miami, FL, AIAA Paper 2007-4473.
[26] Liou, M.S., A Sequel to AUSM, Part II: AUSM+-up for All Speeds, Journal of Computational Physics, Vol.214, pp.137-170, 2006.
[27] Shima, E. & Kitamura, K., On New Simple Low-Dissipation Scheme of AUSM-Family for All Speeds, 47th AIAA Aerospace Sciences Meeting, Orlando, FA, January 5-8 2009, AIAA Paper 2009-136.
[28] Shima, E. & Kitamura, K., On AUSM-Family Scheme for All Speeds with Shock Detection for Carbuncle-Fix, 19th AIAA CFD, 22-25 June 2009, San Antonio, Texas, AIAA Paper 2009-3544.
[29] Saito, S., A Study of Helicopter Gust Response Alleviation by Automatic Control, NASA TM 85870, December , 1983.
[30] Kobiki, N., Saito, S., Kosaka, M., Fuse, H., A Study of Closed Loop Control of Active Tab with BVI Detection Method for Helicopter Noise Reduction, 32nd European Rotorcraft Forum, Maastricht, The Netherlands, September 12-14, 2006.
[31] Kobiki, N., Saito, S., Fuse, H., A Study of Closed Loop Control for BVI Noise Reduction by Multiple pressure sensors, 33rd European Rotorcraft Forum, Kazan, Russia, September 11-13, 2007.
[32] Kobiki, N., and Saito, S., Performance Evaluation of Full Scale On-Board Active Flap System in Transonic Wind Tunnel. American Helicopter Society 64th Annual Forum, Montreal, Canada, April 2008.
[33] Saito, S., Kobiki, N., Tanabe, Y., Johnson, W., Yamauchi, K. G., Young, A.L., Overview of the Novel Intelligent JAXA Active Rotor Program, HeliJapan 2010, Omiya, November 1~2, 2010.
[34] Murahige, A., Kobiki, N., Tsuchihashi, A., Tsujiuchi, T., Inagaki, K., Yamakawa, E., Final Report of ATIC Model Rotor Test at DNW, American Helicopter Society 57th Annual Forum, Washington, DC, May 9-11, 2001.
[35] Aoki, M., Kobiki, N., Yamakawa, E., Saito, S., Shigemi, J., Sato, M. and Kanda, M., Study of High Peroformance /Low Noise Airfoil for a Helicopter Blade, NAL-TM 730,、July, 1998.
[36] Tsujiuchi, T., Tsuchihashi, A., Inagaki, K., Saito, S., Sato, M., Kanda, H., Toda, N., Study on High Performance/Low Noise Airfoil of Helicopter Blade (2nd Report) – Second Two-Dimensional Transonic Wind Tunnel Tests - , NAL TM-759, 2001.
[37] Azuma, A. and Kawachi, K., Local Momentum Theory and Its Application to a Rotary Wing, AIAA 75-865, 1975.
[38] Azuma, A. and Kawachi, K., Local Momentum Theory and Its Application to a Rotary Wing, Journal of Aircraft, Vol. 16, No. 16. pp.6-14, 1979.
[39] A. Azuma, K. Nasu and T. Hayashi, An Extension of the Local Momentum Theory to Rotors Operating in a twisted Flow Field, Vertica, Vol. 7, pp. 45-59, 1983.
[40] Azuma, A. and Saito, S., Study of Rotor Gust Response by means of the Local Momentum Theory, Journal of American Helicopter Society, January, 1982.
[41] S. Saito, A. Azuma and M. Nagao, "Gust Response of Rotary Wing and Its Alleviation," Vertica, Vol. 5, No. 2, pp. 173-184, 1981.
[42] Azuma, A., Saito, S., Kawachi, K. and Karasudani, T., "Application of the Local Momentum Theory to the Aerodynamic Characteristics of Multi-Rotor Systems," Vertica, Vol. 3. pp. 131-144, 1979.
[43] S. Saito and A. Azuma, "A Numerical Approach to Co-axial Rotor Aerodynamics," Vertica, Vol. 6. pp. 253-266, 1982.
[44] K. Nasu, and A. Azuma, An Experimental Verification of the Local Circulation Method for a Horizontal Axis Wind Turbine, 18th Inter Society Energy Conversion Engineering Conference, pp. 21-26, August, 1983.
[45] K. Nasu, S. Saito, H. Kobayashi and Y. Nakamura, "Extension of Local Circulation Method to Counter Rotation Propeller, SAE 87-1891.
[46] S. Saito, H. Kobayashi and Y. Nakamura, Performance Calculation of Counter Rotation Propeller, SAE 87-1889.
[47] A. Azuma, S. Saito and K. Kawachi, "Response of a Helicopter Penetrating the Tip Vortex of a Large Airplane," Vertica, Vo. 11, pp. 65-76, 1987.
[48] Luo, H., Baum, J. & Lohner, R., On the Computation of Multi-Material Flows Using ALE Formulation, Journal of Computational Physics, Vol.194, pp.304–328, 2004.
[49] Zhang, L.P. & Wang, Z.J., A Block LU-SGS Implicit Dual Time-Stepping Algorithm for Hybrid Dynamic Meshes, Computers & Fluids, Vol.33, pp.891–916, 2004.
[50] Wright, M.J., Candler, G.V. & Prampolini, M, Data-Parallel Lower-Upper Relaxation Method for the

Navier-Stokes Equations, AIAA Journal, Vol.34, No.7, July 1996, pp.1371-1377.
[51] Shima, E. & Jounouchi, T., Role of CFD in aeronautical engineering (No.14) - AUSM type upwind schemes - , NAL SP-34, 1999, pp.7-12.
[52] Tanabe, Y. & Saito, S., A Simplified CFD/CSD Loose Coupling Approach for Rotor Blade Deformation, JAXA-RR-08-008E, 2009.
[53] Yamamoto, S. and Daiguji, H., Higher-Order-Accurate Upwind Schemes for Solving the Compressible Euler and Navier-Stokes Equations, Computers & Fluids, Vol.22, No.2/3, pp.259-270, 1993.
[54] Tanabe, Y., Shigeru Saito, S., Kobiki, N., Murota, K., Sugawara, H., Kyohei Hayashi, H. and Hiraoka, K., An Experimental Study of Rotor/Fuselage Interaction, 35th European Rotorcraft Forum, Hamburg, Germany, September 22-25, 2009.
[55] Tanabe, Y., Saito, S. and Otani. I., Numerical Simulations of Rotor/Fuselage Interactions Utilizing an All-Speed Scheme, 2nd International Forum on Rotorcraft Multidisciplinary Technology, Seoul, Korea, October 19-20, 2009
[56] Takayama, O., Sasaki, D., Nakahashi, K., Tanabe, Y. and Saito, S., Coupling Method of Unstructured and Structured Grids for Flow Around ROBIN Configuration, 2nd International Forum on Rotorcraft Multidisciplinary Technology, Seoul, Korea, October 19-20, 2009.
[57] Tanabe, Y. and Saito, S., Experimental and Numerical Studies of Rotor/Fuselage Interactions, American Helicopter Society Aeromechanics Specialists' Conference, San Francisco, California, Jan. 20-22, 2010.
[58] Tanabe, Y. and Saito, S., Validation of a New Rotor Flow Code Using JMRTS Experimental Data, American Helicopter Society 66th Annual Forum, Phoenix, AZ, May 11-13, 2010
[59] Tanabe, Y., Saito, S., Takayama, O., Sasaki, D., and Nakahashi, K., A New Hybrid Method of Overlapping Structured Grids Combined with Unstructured Fuselage Grids for Rotorcraft Analysis, 36th European Rotorcraft Forum, Paris, September 7-9, 2010
[60] Tanabe, Y. and Saito, S., Improvements in Noise Prediction For Rotorcraft, HeliJapan 2010, Omiya, November 1-2, 2010.
[61] Saito, S., Study of Gust Response of a Helicopter, Doctoral Thesis, March, 1980.
[62] Saito, S., Tanabe, Y., Yang, C. and Aoyama, T., Hashimoto, A. and Nakamura, Y., Aeroelastic Simulation of HARTII Model Using Moving Overlapped Grid Approach, 32nd European Rotorcraft Forum, Maastricht, The Netherlands, September 12-14, 2006.
[63] Myklestad, N.O., Fundamentals of Vibration Analysis, McGraw-Hill Book Company inc., New York, 1944.
[64] Myklestad, N.O., A New Method of Calculation Natural Modes of Uncoupled Bending Vibration of Airplane Wings and Other types of Beams, Journal of Aeronautical Sciences, April, 1944.
[65] Bisplinghoff, R. L., Ashley, H. and Halfman, R. L.: Aeroelasticity. Addition-Wesley Publishing Company Inc., Cambridge, Mass., 1955.
[66] Kato, K. and Yamane, T., A Calculation of Rotor Impedance for Hovering Articulated-Rotor Helicopters, Journal of Aircraft, Vol. 16, No. 1, January 1979, pp.15-22.
[67] Tanabe, Y., Saito, S., A Simple CFD/CSD Loose Coupling Approach For Rotor Blade Aeroelasticity, 33rd European Rotorcraft Forum, Kazan, Russia, September 11-13, 2007.
[68] Lim, J.W., Nygaard, T.A., Strawn, R. and Potsdam., M., BVI airloads prediction using CFD/CSD Loose Coupling, American Helicopter Society 4th Vertical Lift Aircraft Design Conference, San Francisco, CA, January 2006.
[69] Tanabe, Y. & Saito, S., A Simplified CFD/CSD Loose Coupling Approach for Rotor Blade Deformation, JAXA-RR-08-008E, 2009
[70] Johnson, W., Self-Tuning Regulators for Multicyclic Control of Helicopter Vibration, NASA TP-1996, March 1982.
[71] Lighthill, M.J., On sound Generated Aerodynamically : I. General Theory, Proceedings of the Royal Society of London, Series A: Mathematical and Physical Sciences, Vol.211, No.1107, 1952, pp.564-587.
[72] Farassat, F., Theory of Noise Generation from Moving Bodies with an Application to Helicopter Rotors, NASA TR R-451, 1975.
[73] Farassat, F., Discontinuities in Aerodynamics and aeroacoustics: The concept and Applications of Generalized Derivatives, Journal of Sound and Vibrations, Vol.55, No.2, 1977.
[74] Ffowcs Williams, J.E. et al, Sound Generation by Turbulence and Surface in Arbitrary Motion, Philosophical Trans. of the Royal Society of London, Series A, Vol.264, 1969, pp.21-342.
[75] Nakamura, Y., et al, Rotational Noise of Helicopter Rotors, Vertica, Vol.3, No.3/4, 1979, pp.293-316.